ISSN NO. 0737-5352-17

THE WIND'S RESPONSE TO TRANSIENT MESOSCALE PRESSURE FIELDS ASSOCIATED WITH SQUALL LINES

CIRA Cooperative Institute for Research in the Atmosphere

Michael D. Vescio

Colorado State University

THE WIND'S RESPONSE TO TRANSIENT MESOSCALE PRESSURE FIELDS ASSOCIATED WITH SQUALL LINES

by

Michael D. Vescio

Department of Atmospheric Science
Colorado State University
Fort Collins, CO 80523

This research was supported by NOAA
under Grant No. NA 85 RAH 05045 through CIRA

May 1990

ABSTRACT OF THESIS

THE WIND'S RESPONSE TO TRANSIENT MESOSCALE PRESSURE FIELDS ASSOCIATED WITH SQUALL LINES

A simple one-dimensional slab model has been developed to examine the wind's response to transient mesoscale pressure fields that frequently accompany mature midlatitude squall lines. The model numerically solves a form of the momentum equation that includes the pressure gradient force, advection, and the frictional force. The Coriolis force is neglected since attention is focused on time periods of 1–2 hrs. The pressure field is specified by a sine wave with a constant phase speed. The amplitude of this wave is initially zero, but then increases linearly with every timestep until $t = 2$ hrs. At this time, the wave reaches its predetermined maximum amplitude. This pressure wave represents a mesohigh and wake low that have the same amplitude and phase speed.

Since these features are transient, the air lacks sufficient time to achieve a balanced state. Therefore, winds are directed forward through the mesohigh, and rearward through the wake low, at right angles to the isobars. This airflow pattern produces an axis of divergence to the rear of the mesohigh, with convergence occurring near the back edge of the wake low. The model is able to accurately simulate the airflow near these pressure features. Pressure waves with various maximum amplitudes and phase speeds are used in the model for the purpose of comparison. Model results vary slightly as the phase speed and maximum amplitude of the pressure wave is changed. Air parcel trajectories are used to help explain these variations.

Model results are compared to the observed airflow near the mesohigh and wake low associated with an intense squall line that moved through Oklahoma and Kansas on 10–11

June 1985. The time period of interest is 0100–0400 UTC on the 11th of June, during which the squall line, as well as the mesoscale pressure fields, reached their maximum intensity. Cross sections through the center of the mesohigh and wake low indicate that the pressure field was roughly sinusoidal with an amplitude of approximately 2.5 mb. Therefore, model results obtained using a 2.5 mb maximum amplitude pressure wave are used for this comparison. The model derived wind field is similar to the observed wind field in many respects. Differences can be attributed to several factors, one of which is the fact that the pressure field, specified in the model, is only an approximation to the observed pressure field.

Finally, a discussion of the frictional force is presented. To assess the relative importance of the surface friction term, a scale analysis of the momentum equation is performed. This analysis shows that this term is only one order of magnitude smaller than the next smallest term in the momentum equation. Therefore, surface friction cannot be neglected. Slight variations in model results occur as the magnitude of this term varies. The effects of momentum transport from above on the surface wind field are also discussed. It appears that such transport is only important near the leading convective line where convective scale updrafts and downdrafts are occurring. Behind the convective line, the rain cooled air is much too stable, and the convective scale motion is too weak, for significant momentum transport into the boundary layer.

ACKNOWLEDGEMENTS

I wish to extend my sincere gratitude to my advisor Dr. Richard H. Johnson. Without his guidance and support, this work would not have been possible. Additional thanks are extended to my other committee members, Dr. Wayne Schubert, and Dr. William Duff.

Special appreciation is given to two of my colleagues, James Bresch and William Gallus, who spent a great deal of time answering the numerous questions that I had pertaining to my research and the computer facilities. Their input was truly valuable.

I would also like to thank those who helped me in many different ways during my stay at Colorado State, including Gail Cordova, Ben Bernstein, Greg Stumpf, Jim Staley, and Fredell Boston.

This research was supported by the National Oceanic and Atmospheric Administration through CIRA under grant NA 85 RAH 05045.

TABLE OF CONTENTS

LIST OF FIGURES

LIST OF TABLES

Chapter 1

INTRODUCTION

It has been known for many years that organized mesoscale convective systems (MCSs), such as squall lines, can affect the surface pressure field. Frequently, distinct surface pressure features accompany the MCS in the form of mesohighs and mesolows (ahead of, and to the rear of, the mesohigh). These features are often associated with strong pressure gradients. Pressure rises (falls), at a particular location, may be 2–6 *mb* or more in as little as 5 min (Williams 1948, 1953).

To begin with, the mesohigh, which is generally located just to the rear of the leading edge of convection, has been well documented [*e.g.* Sawyer (1946), Byers and Braham (1949), Tepper (1950), Fujita (1955, 1959), Williams (1948, 1953), Pedgley (1962), Fritsch and Chappell (1980), Stumpf (1988), and Johnson and Hamilton (1988)]. Fujita (1959) attributed the mesohigh to rainfall evaporation and the melting of ice particles (hail) in convective downdrafts. The cooling due to evaporation and melting produces hydrostatically higher pressures near the surface beneath the downdrafts. Fujita also mentions that part of the surface pressure rise may be due to non-hydrostatic effects as well. Downdraft air striking the surface may cause slight rises in pressure. Earlier work by Schaffer (1947) indicates that the non-hydrostatic pressure rise is relatively small compared to the hydrostatic pressure increase.

A mesolow is often found trailing the mesohigh. It is generally located at the back edge of where the stratiform rain, in the rear portion of the squall line, reaches the ground. It usually develops well after the formation of the mesohigh during the mature to decaying stages of the MCS.[1] This feature has also been the subject of much study [*e.g.* Brunk (1953), Fujita (1955), Williams (1953, 1954, 1963), Pedgley (1962), Fritch and Chappell (1980), Koch and McCarthy (1982) Stumpf (1988), and Johnson and Hamilton (1988)]. Some of the early terminology referring to this low included "pressure pulsation" (Brunk, 1953), "depression-type wave" (Tepper, 1950) and (Williams, 1954), and "wake depression" (Fujita, 1955). More recently, the name "wake low" has been given to this surface pressure feature.

The dynamics that are necessary for the formation of the wake low are not fully understood, although evidence suggests that its presence is a result of strong subsidence warming at the rear of the squall line. Williams (1963) first demonstrated that subsidence warming can account for the pressure falls associated with the wake low. His study of a thunderstorm wake that occurred on 4 May 1961, revealed a warm dry airflow descending at the rear of the convective line. Williams, however, did not explain the mechanism that would cause such subsidence. Zipser (1977) found anomalous low θ_w air above the mixed layer to the rear of several tropical squall lines. This air must have descended from a level (approximately 750 mb) where this θ_w was common. Zipser speculated that this air could enter the squall line from any direction.

Recent studies suggest that this descending mid-level dry air enters the squall line from the rear. This rear-inflow jet has been observed in a number of squall lines studied by Smull and Houze (1987). Rutledge *et al.* (1988) studied the structure of an intense squall line occurring on 10–11 June 1985 (the surface pressure features associated with this squall line will be examined in this study) with single Doppler radar data. Their analysis indicated that a strong rear-inflow jet was present with this convective system for several hours. The inflow entered the storm at about 10 km above sea level, and eventually descended below the melting level (0°C) as it entered the stratiform region of the squall line. Figure 1.1 displays this process schematically. Johnson and Hamilton

[1]Often mesolows are found ahead of the squall line, hence the name pre-squall mesolow. This feature is not directly related to this study. Therefore, it is not discussed in the text. For more information on this feature, see Johnson and Hamilton (1988).

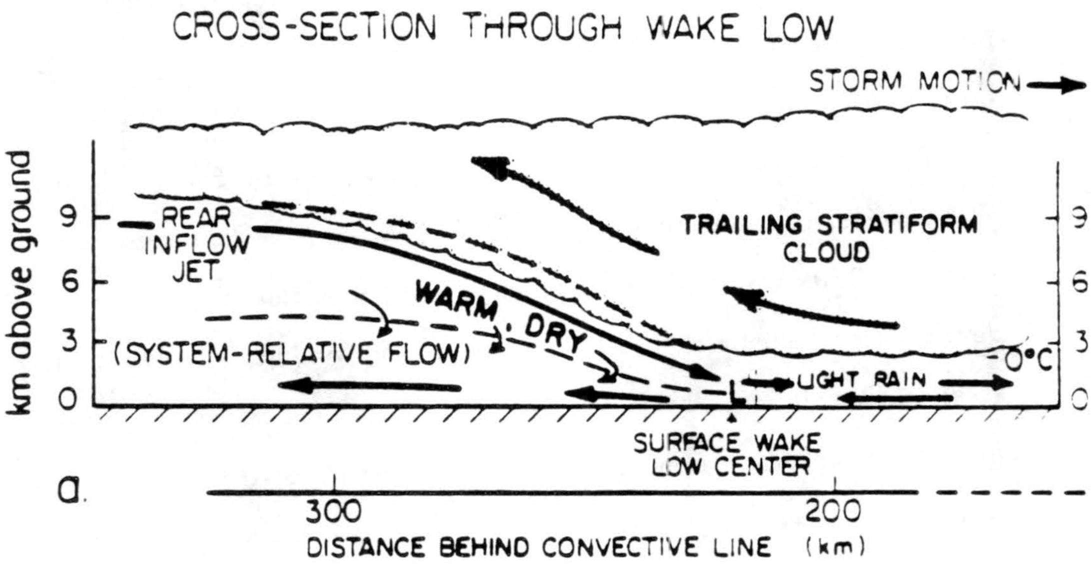

Figure 1.1: A schematic cross section through the stratiform portion of an MCS (from Johnson and Hamilton, 1988).

(1988) believe that the wake low is a surface manifestation of the rear-inflow jet. As the jet descends, warming and drying occur. The maximum warming and drying is observed at a height of about 1 km, at the back edge of the stratiform rain area. The greatest pressure reduction, due to hydrostatic effects, occurs at this location. As the rear-inflow jet penetrates the stratiform rain area, warming and drying (hence pressure reduction) diminishes as evaporative cooling increases.

It is speculated that the driving force for this rear-inflow jet is a mesolow at mid-levels in the stratiform region of the MCS. In a numerical study, Brown (1979) noticed the formation of a pronounced mid-level mesolow in the stratiform portion of the MCS. This low is attributable to latent heating aloft in the trailing anvil and evaporative cooling at lower levels as precipitation falls through a subsaturated environment. The pressure gradient associated with this low could be responsible for the development of rear-inflow into the system.

The surface airflow in the vicinity of these pressure fields is highly ageostrophic. Williams (1954) noticed that the winds near these features did not conform to the pressure gradient. Winds were observed to blow at right angles to the isobars. Fujita (1955) developed a schematic of the surface pressure and wind fields observed during the mature stage of a squall line. This is displayed in Fig. 1.2. The instantaneous airflow is directed forward through the mesohigh with a diffluence axis located to the rear of the high center. A wake low (or wake depression) is found to the rear of the mesohigh with air converging in its center. Observations of Johnson and Hamilton (1988), suggest a flow that is somewhat different. Their observations are presented in Fig. 1.3. The air flow associated with the mesohigh is the same as Fujita's. However, in the case of the wake low, air is not converging in its center. The instantaneous airflow is directed rearward through the wake low with a confluence axis near the back edge of this pressure feature. The ageostrophic flow near these pressure fields result from their transient nature (Garratt and Physick, 1983). Since these features are unsteady, (*i.e.*, their pressure gradients are not in a steady-state) air does not have sufficient time to attain geostrophic balance. Therefore, an airflow, normal to the isobars, towards low pressure results. However, since these features are moving, the

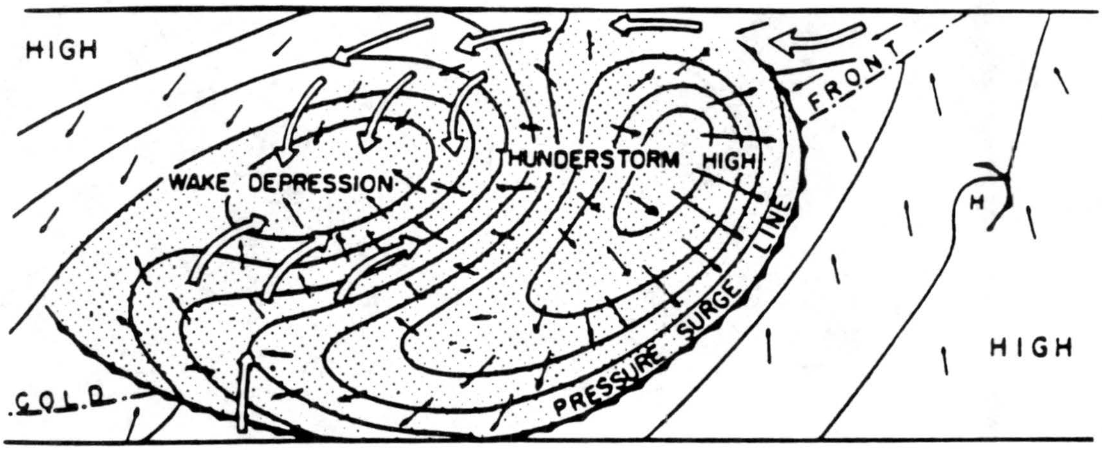

Figure 1.2: Surface pressure fields associated with a mature squall line (from Fujita, 1955).

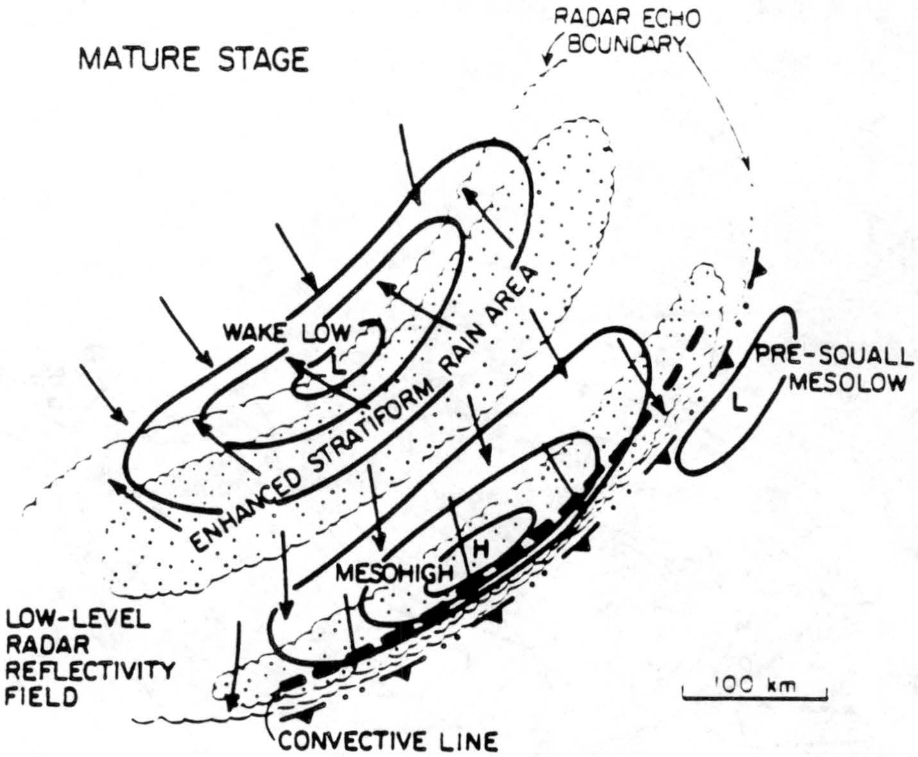

Figure 1.3: Surface pressure and wind fields, along with precipitation distribution, during the mature stage of a midlatitude squall line (from Johnson and Hamilton, 1988).

instantaneous wind field shows an airflow towards higher pressure for a short distance to the rear of the mesohigh and wake low axes.[2] It takes time for air parcels, once located to the rear of the mesohigh or wake low, to decelerate and reverse directions. During this time, the pressure system has moved downstream.

Garratt and Physick (1983) studied mesoscale pressure features that occur with convective systems over southern Australia through the use of a one-dimensional slab model similar to the one used by Mahrt (1974). The slab model is advantageous to a more complicated model, in some respects, since realistic results can be obtained without the inclusion of stress parameterizations. Although the use of this model eliminates the vertical structure of the boundary layer, for a relatively thin layer of atmosphere, the slab model should produce layer-averages that are representative of the flow at a given level. This is the case when the low-level vertical wind shear is weak. One might expect strong vertical wind shear with these pressure features. However, Garratt and Physick indicate that significant shear does not have time to develop since these features are transient.

The model they used essentially solved a form of the momentum equation that included the pressure gradient force and friction. They assumed that there was no y variation in surface properties. Therefore, the vector form of the momentum equation reduced to an equation that could be used to solve for the u-component. The model derived wind field resembled the observed winds associated with these pressure features. However, a serious limitation of Garratt and Physick's study is their neglect of horizontal advection in the momentum equation. They argued that advection was small compared to the pressure gradient force and therefore could be neglected. A scale analysis presented in chapter 8 will show that neglecting the advection term is unjustifiable for these pressure features since its magnitude may, in some cases, be equivalent to the pressure gradient force.

For this study, a one dimensional slab model has been developed that is similar to (but developed independently from) the one discussed in Garratt and Physick (1983). The

---

[2]It will be shown in chapter 4 that this distance is proportional to the phase speed of the pressure disturbance.

model is used to examine the wind's response to a transient mesoscale pressure wave. This wave is sinusoidal and represents the mesohigh wake low couplets that are often associated with mature midlatitude squall lines. The model is run using pressure waves with different amplitudes and phase speeds, to determine how the wind field varies with faster (slower) moving and more (less) intense pressure fields. Air parcel trajectories are constructed through these pressure waves to help explain the airflow pattern displayed in Fig. 1.3. They are also used to explain the variations in the airflow that result when using pressure waves with different amplitudes and phase speeds in the model.

Model derived wind fields are compared to the wind fields associated with a mesohigh and wake low that occurred in conjunction with an intense squall line, with a trailing stratiform region, that moved through Oklahoma and Kansas on 10–11 June 1985. The squall line moved through the OK PRE-STORM (Oklahoma-Kansas Preliminary Regional Experiment for STORM-central) data network. This field experiment, conducted in May and June 1985, provided an excellent data set to study the evolution and structure of mesoscale convective systems. Surface observations had a spatial and temporal resolution of 50 km and 5 min respectively. These space and time scales were small enough to study the mesohigh and wake low, as well as, the airflow associated with these pressure features. It will be shown that the model derived wind and divergence fields are similar to those observed with this particular MCS.

The relative importance of the frictional force is determined through a scale analysis of the momentum equation. The model's sensitivity to surface friction is also discussed by examining results with various magnitudes of this term. Finally, a term due to momentum transport at the model layer top is added to the momentum equation, to determine the role, if any, of momentum transfer in determining the wind field near these pressure fields.

Chapter 2

THEORY AND NUMERICAL METHODS

2.1 The momentum equation

The momentum equation can be written as:

$$\frac{d\mathbf{V}}{dt} = -2\mathbf{\Omega} \times \mathbf{V} - \frac{1}{\rho}\nabla \mathbf{p} + \mathbf{g} + \mathbf{F} , \qquad (2.1)$$

where boldface type indicates a vector quantity. The first term on the right-hand-side (RHS) of (2.1) represents the Coriolis force with $\mathbf{\Omega}$ being the earth's rotation rate. The second, third, and fourth terms are the pressure gradient force, gravity, and the frictional force respectively. Equation (2.1) can be written in component form to yield individual equations in u, v, and w.

In the model, a coordinate system has been adopted such that u is the component of the wind normal to the axis of the mesoscale pressure fields under investigation (negative u indicating flow from the east and positive from the west). Using the Boussinesq approximation, a vertically integrated form of (2.1) for a shallow layer near the earth's surface can be written as:

$$\frac{\partial u_m}{\partial t} = -\frac{1}{\rho}\frac{\partial p_m}{\partial x} - \mathbf{V}_{hm} \cdot \nabla u_m + f v_m + \frac{1}{H}\int_0^H F dz , \qquad (2.2)$$

where $f = 2\Omega\sin\phi$, and F, the friction term $= -\frac{\partial}{\partial z}\overline{u'w'}$. The subscript m denotes vertically integrated values, the subscript h refers to the horizontal wind components (u and v), H represents the depth of the pressure disturbance, overbar refers to a horizontal average and prime the deviation from that average.

A few assumptions are made to obtain (2.2). First, the horizontal eddy flux convergence of momentum $(-\frac{\partial}{\partial x}\overline{u'u'}, -\frac{\partial}{\partial y}\overline{u'v'})$ is considered small compared to $-\frac{\partial}{\partial z}\overline{u'w'}$ and is therefore neglected. Also, since w_m is small near the earth's surface, $w_m\frac{\partial u_m}{\partial z}$ is smaller than the other advective terms and it too is neglected.

Since these pressure fields are quasi-two dimensional with the line-normal velocities (u) much larger than the line-parallel velocities (v), $v\frac{\partial u}{\partial y} \ll u\frac{\partial u}{\partial x}$ and can be neglected. Also, the Coriolis force (fv) can be eliminated since attention will be focused on accelerations over a 1–2 hour period, which is less than the time scale for the Coriolis force ($\frac{1}{f}$) for midlatitudes. With these additional assumptions, the momentum equation can now be written (omitting the subscript m):

$$\frac{\partial u}{\partial t} = -\frac{1}{\rho}\frac{\partial p}{\partial x} - u\frac{\partial u}{\partial x} + \frac{1}{H}\int_0^H F dz\ . \tag{2.3}$$

This equation was used to calculate u in the model and will be expressed in finite difference form, excluding the friction term, in Section 2.3. The friction term will be expanded in Section 3.4. Equation (2.3) is essentially the same as the equation developed by Garratt and Physick (1983), except that horizontal advection is included.

2.2 Finite differencing

Numerical techniques are often employed to approximate the solutions to non-linear partial differential equations such as (2.3). Up until the mid 1950's, when the spectral method was developed, finite differencing was used exclusively in numerical weather prediction (see Silberman 1954, Kubota 1959, and Ellsaesser 1966 for discussion of the spectral method). Advantages of the finite difference method over the spectral method include easy computer coding and conceptual simplicity (Pielke, 1984). For these reasons, the finite difference approach, rather than the spectral method, was used in this study to approximate (2.3).

2.3 Finite difference schemes

In a finite difference scheme derivatives are replaced by finite differences to produce an equation that can be solved algebraically. The first few terms in the Taylor series expansion are used to develop finite differences in the following manner:

$$f(x+\Delta x) = f(x) + f'(x)\Delta x + f''(x)\frac{\Delta x^2}{2} + f'''(x)\frac{\Delta x^3}{3!}\,, \tag{2.4a}$$

$$f(x-\Delta x) = f(x) - f'(x)\Delta x + f''(x)\frac{\Delta x^2}{2} - f'''(x)\frac{\Delta x^3}{3!}\,. \tag{2.4b}$$

Using the first 3 terms on the RHS of (2.4a) and solving for $f'(x)$ yields:

$$f'(x) = \frac{f(x+\Delta x) - f(x)}{\Delta x} - \frac{f''(x)\Delta x}{2}\,. \tag{2.5}$$

Dropping the second term in (2.5) yields the *forward difference scheme* whose truncation error $\sim -\frac{f''(x)\Delta x}{2}$. This scheme is considered to be ***first order accurate*** or $O(\Delta x)$.

Subtracting (2.4b) from (2.4a) produces the *centered difference scheme* which is as follows:

$$f'(x) = \frac{f(x+\Delta x) - f(x-\Delta x)}{2\Delta x} - f'''\frac{\Delta x^2}{6}\,. \tag{2.6}$$

Again, dropping the second term in (2.6) produces a truncation error $\sim -f'''\frac{\Delta x^2}{6}$, which makes the centered difference equation *second order accurate* or $O(\Delta x^2)$.[3]

At first glance it would seem that the forward difference scheme would be the most logical approach to time differencing. However, it was just shown that the centered difference scheme produces a higher degree of accuracy with little increase in complexity. Another detriment to the forward scheme is that this method is unconditionally unstable. It has been shown by Thompson (1961) and Pielke (1984) that the solutions to a forward difference scheme are *always* amplifying with time, regardless of the time step and grid spacing used.

For these reasons, forward time differencing was not used in this study. Instead the momentum equation was approximated using a centered in time, which is called the *leapfrog scheme*, as well as centered in space, finite difference equation (FDE). The following equation is the FDE analogous to (2.3):

---

[3]For a complete discussion of finite difference schemes and how they are derived, see Haltiner and Williams (1980).

$$u_i^{k+1} = u_i^{k-1} - \frac{\Delta t}{\Delta x}[\frac{1}{\rho}(p_{i+1}^{k+1} - p_{i-1}^{k+1}) + u_i^k(u_{i+1}^k - u_{i-1}^k)] + \frac{2\Delta t}{H}\int_0^H F dz \,. \qquad (2.7)$$

Here the index k refers to time, while i refers to space. This equation was coded in the model to predict u.

2.4 Filtering of the computational mode

Although the leapfrog scheme is considered more accurate than the forward time scheme, it is not without flaws. Equation (2.3) is first order in time, but (2.7), which approximates (2.3), is second order in time. This causes a non- physical, or computational, mode to appear in the solution of the FDE. The computational mode "*contaminates*" the true solution (*i.e.* the physical mode) by propagating in the opposite direction of the true wave solution. This mode also changes sign with every time step.

To eliminate the computational mode, a time filter must be applied. Asselin (1972) discussed a filter that quickly removes the computational mode from solutions derived from the leapfrog scheme. The equation for this filter as it was used in this study is:

$$u_c^k = u^k + 0.5\nu\,[u^{k-1} - 2u^k + u^{k+1}]\,, \qquad (2.9)$$

where k, once again, is the time index, u_c is the corrected u component, and ν is the filter parameter. This filter was used at every time step.

Chapter 3

MODEL OF TRANSIENT PRESSURE DISTURBANCES ASSOCIATED WITH SQUALL LINES

3.1 Model description

A simple model has been developed to examine the wind's response to a transient pressure wave moving at a constant phase speed. The model essentially predicts u from (2.7). Horizontal divergence was then calculated from the u field. As mentioned in section 2.1, $w_m \frac{\partial u_m}{\partial z}$ is neglected, therefore the solution to (2.7) essentially gives a mean wind ($\bar{u}$) in a layer of atmosphere with depth H. This depth was assumed to be the pressure disturbance depth, which was set at 500 meters when comparing model results with the observations of 10-11 June. H appears in the expression for the friction term in (2.2). Thus as H varies, so does friction. Chapter 8 discusses the model's sensitivity to various magnitudes of the friction term.

3.2 Model parameters

3.2.1 Grid spacing, time step, and computational stability

Choosing a grid spacing is somewhat arbitrary, but the spacing must be small enough to resolve the features that are being modeled. In this case, as will be shown in the next chapter, strong gradients of u and divergence were present in the model results. Therefore, a relatively small grid spacing of 5 km was used to get adequate resolution of these features. Also, Haltiner and Williams (1980) state that the solution to the FDE will approach the true solution when $\frac{\Delta x}{\lambda} \ll 1$, where λ is the wavelength of the disturbance under investigation. This expression simply states that λ should span several gridpoints. It makes sense that the more gridpoints used to describe the disturbance, the better the resolution, which should yield a closer approximation to the true solution. Figures 3.1–3.4 display cross sections of pressure in one hour intervals from 0100–0400 UTC on the 11th. These cross sections were chosen so that they would intersect both the mesohigh and wake low. The zero line in pressure perturbation was found by averaging the highest pressure in the mesohigh and the lowest pressure in the wake low. The figure indicates that the pressure disturbance had a wavelength of approximately 200 km, especially early in the period, and, roughly,a sinusoidal shape. For these reasons, the pressure wave in the model was sinusoidal with a wavelength of 200 km. This combination of Δx and λ gives a $\frac{\Delta x}{\lambda} = .025$ which satisfies the condition of Haltiner and Williams (1980).

Once a grid spacing is determined, a time step must be chosen. Courant *et al.* (1928) discovered that the time step and grid spacing can not be chosen independently. Instead, the following expression must be true to guarantee computational stability:

$$c\frac{\Delta t}{\Delta x} < 1 , \tag{3.1}$$

where c is the speed of the fastest wave permitted in the model. This can be up to 300 m s^{-1} if sound and gravity waves are permitted. In this model, however, sound waves are not permitted since density is a constant. Gravity waves are not permitted either since vertical motion is not predicted. Therefore, the fastest speed permitted by the model is the highest value of u generated. For all model runs the maximum u was less than 25 m s^{-1}. This combination of maximum speed, grid spacing, and timestep satisfy (3.1).

3.2.2 Lateral boundary conditions

Boundary conditions were not that critical either, since data was taken from the center portion of the grid only. Since the model was run for only a short time, it is doubtful that any disturbance initiated at the boundary would have sufficient time to enter the center of the grid.

Nonetheless, a simple boundary condition was applied. It was assumed that the u-component one gridpoint from the boundary was the average of the u- component at the gridpoints on either side. This can be expressed for the *left* boundary as follows:

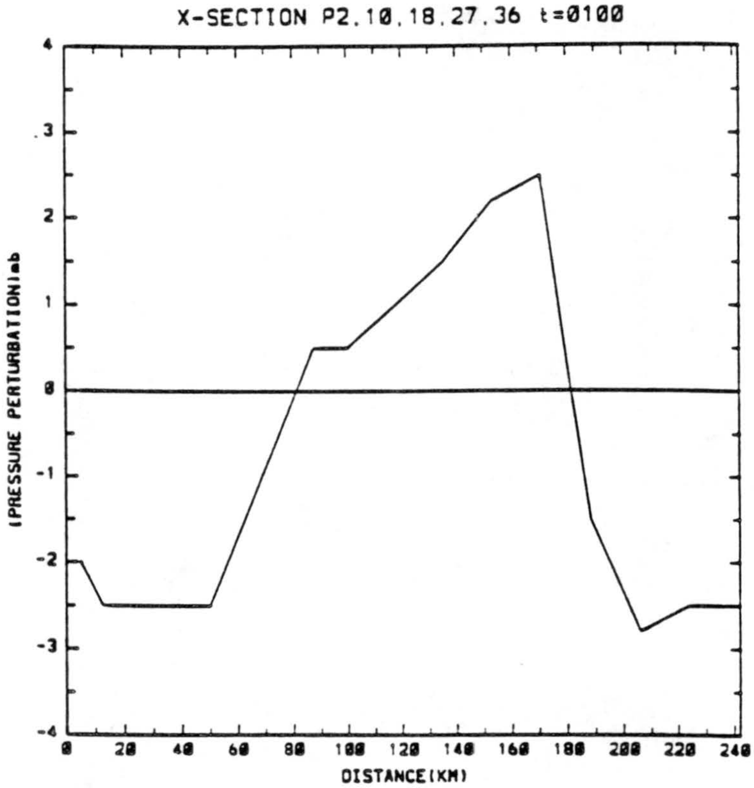

Figure 3.1: Pressure cross section through the wake low and mesohigh at 0100 UTC on the 11th.

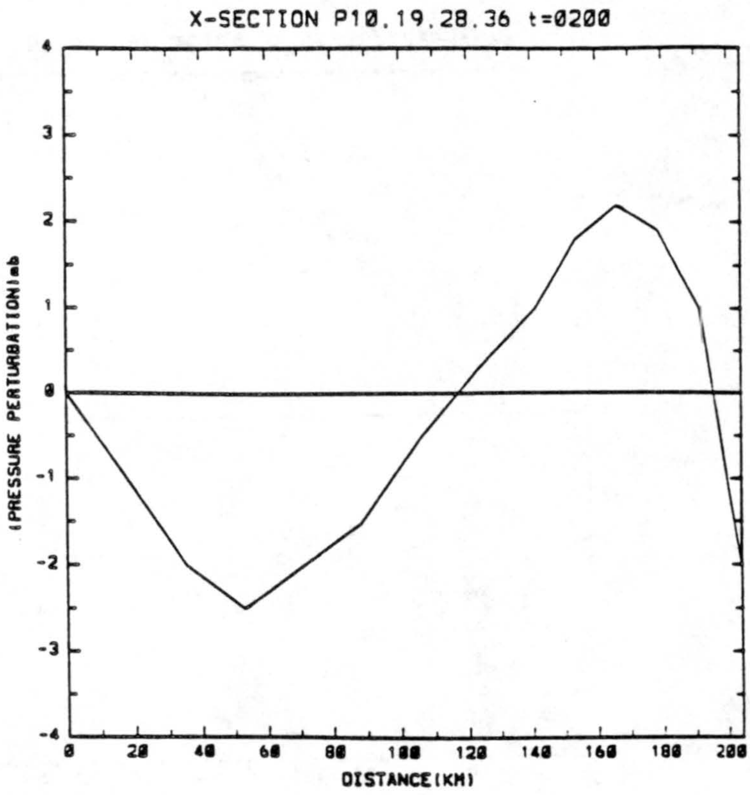

Figure 3.2: Same as Fig. 3.1, except for 0200 UTC.

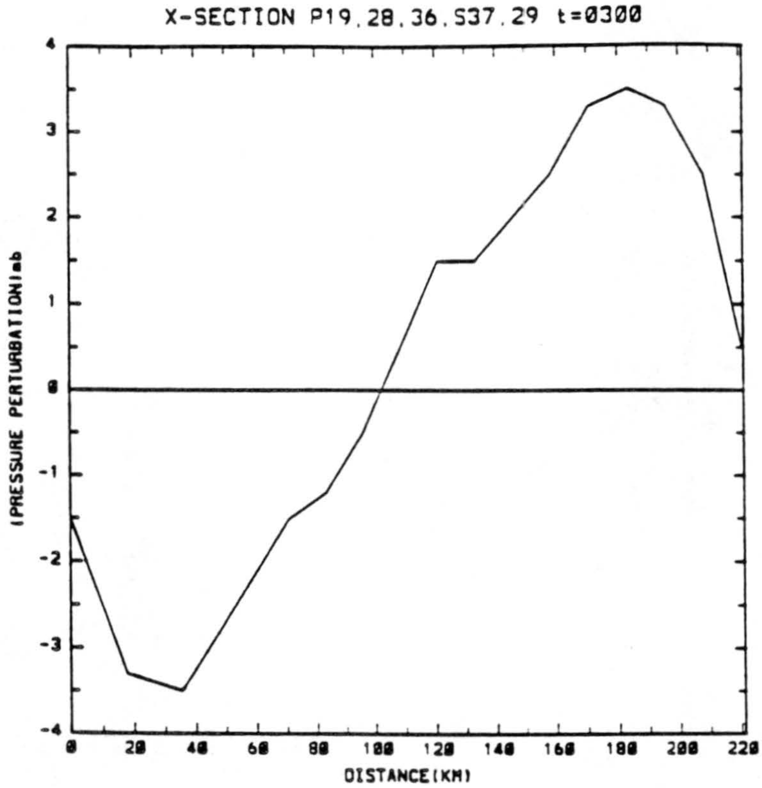

Figure 3.3: Same as Fig. 3.1, except for 0300 UTC.

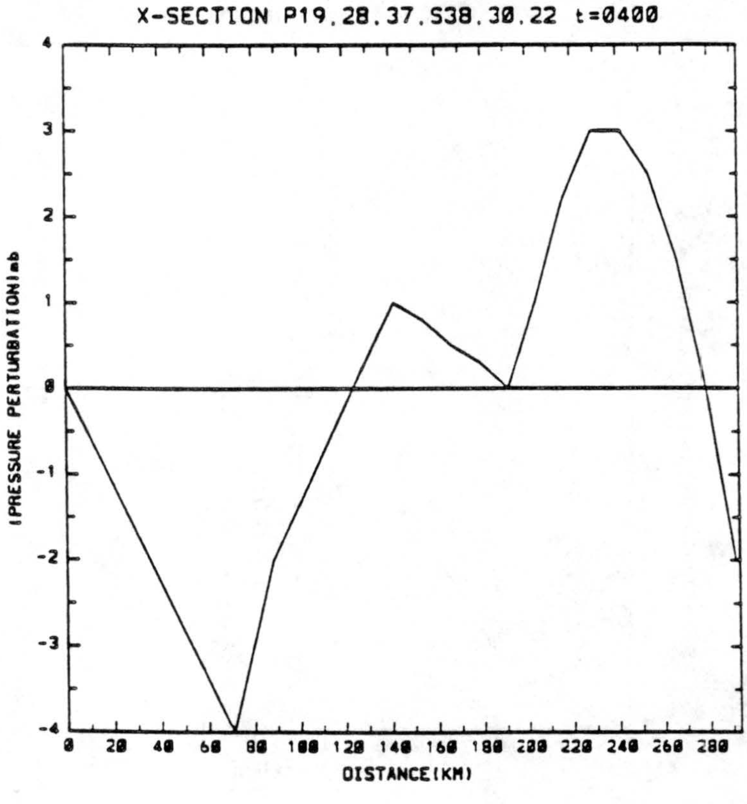

Figure 3.4: Same as Fig. 3.1, except for 0400 UTC.

$$u_2 = \frac{u_3 + u_1}{2} \,, \tag{3.2}$$

where u_1 = the u-component at the left boundary. Since u_2 and u_3 are solved directly in the model, (3.2) can be solved for u_1 so that

$$u_1 = 2u_2 - u_3 \,. \tag{3.3}$$

A similar extrapolation was applied at the right boundary.

3.3 Treatment of the pressure field

As mentioned in the previous section (see fig. 3.1–3.4), the pressure wave associated with the 10–11 June MCS resembled a sine wave with a wavelength of approximately 200 km. The wave's amplitude was somewhat variable, but averaged 2–3 mb. The amplitude of the pressure wave in the model was initially set to zero, but then was increased linearly to 2.5 mb at t = 2 hrs.[4] The function that describes the pressure at a gridpoint is:

$$P = amplitude * sin\left[\frac{2\pi}{L}(x - ct)\right] \,, \tag{3.4}$$

where c = phase speed of the pressure disturbance, L = the wavelength of the pressure wave, and x = gridpoint's position relative to the pressure wave.

The phase speed of the pressure wave was determined from the argument that the mesohigh, which is a reflection of the cold pool associated with the thunderstorm downdraft, is a type of density current. Simpson (1966), Simpson *et al.* (1977), and Charba (1974) first made this hypothesis. These studies, however, were inconclusive due to insufficient data.

Wakimoto (1982) was able to improve upon these studies by using data from Project NIMROD (Northern Illinois Meteorological Research on Downburst) which was conducted during the spring of 1978. He concluded that the movement of the gust front, and

[4]Other runs were made with maximum amplitudes of 1.5 and 3.5 mb and will be discussed in chapter 4.

therefore the mesohigh, could be predicted accurately by the equation governing density current motion. The equation for density current speed used by Wakimoto is:

$$V = k\left(gd\frac{\bar{\rho}_c - \bar{\rho}_w}{\bar{\rho}_w}\right)^{\frac{1}{2}} , \tag{3.5}$$

where g = gravity, d = depth of the outflow, $\bar{\rho}_c$ = mean density in the cold air, $\bar{\rho}_w$ = mean density in the warm air, and k = the internal Froude number. A problem with this equation is that rawindsonde data is required to find d and to calculate $\bar{\rho}_c$ and $\bar{\rho}_w$.

Seitter (1986) developed a new equation describing density current motion that includes only surface parameters and is as follows:

$$V = k\left(\frac{\Delta p}{\rho_w}\right)^{0.5} , \tag{3.6}$$

where Δp = the difference in surface pressure between the density current and the environment, and ρ_w = density at the surface in the warm air ahead of the density current. To determine the value of k, Seitter applied (3.6) to 20 gust fronts whose phase speed was known. From these observations, the best value for k = .79. Using this value of k, a Δp = 5 mb, which is the pressure difference between the axis of the mesohigh and wake low, and a ρ_w = 1.2 kg m^{-3}, gives a density current speed of 16.3 m s^{-1}. This speed is nearly identical to the speed of the convective line (and thus the mesohigh) over Oklahoma for the 10–11 June MCS.

3.4 Frictional force

The equation describing the friction term in the model is:

$$\frac{1}{H}\int_0^H F dz = -\frac{C_D\,|u|\,u}{H} - \frac{\overline{(u'w')}}{H} , \tag{3.7}$$

where the first term on the RHS of (3.7) represents a surface drag, with C_D being the drag coefficient. The second term represents the momentum flux at the top of the model. Newton (1950) has shown that in squall lines systems, vertical transport of momentum in convective scale downdrafts can contribute significantly to the surface winds. This term was neglected in most of the model runs, but it was included in a sensitivity test to assess its relative importance. Results using the full friction equation are discussed in chapter 8.

The drag coefficient (C_D) varies with surface roughness and static stability. Rougher surfaces generally cause more intense turbulence which increases the drag. Also, frictional drag increases with decreasing static stability since a statically unstable atmosphere is conducive to turbulence. As a first approximation to the drag coefficient, the expression for C_d under statically *neutral* conditions (C_{DN}) is:

$$C_{DN} = k^2 \left[ln(\frac{z}{z_o}) \right]^{-2} , \tag{3.8}$$

where z_o = roughness length, and k = von Karman constant. The value of k has not been agreed upon, but most believe that it is in the range of .35 – .4 (Stull, 1988). The height (z) at which this equation applies is also a subject of discussion. Lavoie (1972) calculated drag coefficients at z = 50 m. Instrument shelters measure temperature and moisture at 2 m, whereas surface winds are routinely measured at a slightly greater height. A value of z = 10 m is often used when calculating drag coefficients.

Equation (3.8) was used to calculate a drag coefficient for the model with z = 10 m, and k = .4. Since the terrain in the PRE-STORM network consists primarily of plains, a roughness length (z_o) for this type of surface was used. Panofsky and Dutton (1984) give a z_o of .01 m for fairly level grass plains and .1 m for farmland which yield a $C_{DN} = 3.35 \times 10^{-3}$ and 7.54×10^{-3} respectively. A value between these ranges of 5×10^{-3} was used in the model. As mentioned earlier, (3.8) applies for neutral static stability. Actually conditions behind the convective line are stable (see figure 8.1), thus the drag coefficient may be less than what was calculated. Chapter 8 discusses results with various smaller drag coefficients.

Chapter 4

MODEL RESULTS

In this chapter, results obtained from the numerical model described in chapter 3, are discussed. The model was run with pressure waves with maximum amplitudes of 1.5, 2.5, and 3.5 mb. All three pressure waves had wavelengths of 200 km. Using this information in (3.6) yields phase speeds of 12.6, 16.3, and 19.3 m s^{-1} respectively. The phase speed of each wave was assumed constant with time in every case. This is a valid assumption for application to the 10–11 June squall line since the motion of the initiating convective line was, to a large extent, dictated by an advancing upper-level trough. This trough moved eastward at a nearly constant speed of 15 m s^{-1}. It is also important to note, once again, that the amplitude of the pressure wave was initially set to zero and then increased linearly with every timestep until the wave reached its maximum amplitude at $t = 120$ min. Also, the background, or environmental, pressure gradient was assumed to be flat. Therefore, the initial u field was set to zero. For the results discussed in this chapter, H, the depth of the pressure disturbance, was 500 m, and the drag coefficient, C_d, $= 5 \times 10^{-3}$. Results using the 2.5 mb pressure wave are discussed in detail in the next section since this wave closely resembles the speed and amplitude of the pressure wave associated with the 10-11 June MCS. Results from the other two pressure waves will be compared to the 2.5 mb wave to determine how the wind field responds to a pressure wave with a higher (lower) amplitude and, therefore, a higher (lower) phase speed. Several trends are revealed when comparing model results using the different amplitude pressure waves. A possible explanation for each of these trends is presented.

4.1 Model results with a 2.5 mb pressure wave

Figures 4.1-4.4 display model results at time t = 30, 60, 90, and 120 min for a pressure wave with a maximum amplitude of 2.5 mb. Each figure consists of two parts: part *a* is a plot of pressure and *u*- component, while part *b* is a plot of pressure and divergence. The abscissa is distance in km and is provided to determine the separation or ***phase shift*** of the maximum *u*-component (positive and negative), divergence, and convergence relative to the mesohigh and wake low axes.

To begin with, Fig. 4.1 shows that at t = 30 min, maximum positive *u*-components (i.e. the strongest west winds) are slightly less than 1.5 m s^{-1} and are located ahead of the mesohigh and to the rear of the wake low. A maximum negative *u*-component (i.e. the strongest east wind) of 1.5 m s^{-1} is found 40 km ahead of the wake low. The maximum divergence (negative convergence) at this time is occurring well to the rear of the wake low, with a secondary maximum 10 km to the rear of the mesohigh. Maximum convergence is occurring well ahead of the mesohigh along the simulated gust front, while an area of weaker convergence is located to the rear of the wake low.

At t = 60 min (Fig. 4.2) , the maximum wind speeds are now greater in response to the amplifying pressure wave. The strongest west winds are now approaching 5 m s^{-1} ahead of the mesohigh and to the rear of the wake low. The strongest east winds are 5.2 m s^{-1} at a location 27.5 km ahead of the wake low. Notice that west winds now extend 15 km behind the mesohigh center, and that east winds are found 20 km to the rear of the wake low. This indicates that, in the model, the instantaneous airflow is directed ***forward*** through the mesohigh and ***rearward*** through the wake low. The maximum divergence, at this time, is greater behind the mesohigh than to the rear of the wake low. Likewise, the maximum convergence is now located to the rear of the wake low, rather than along the gust front. The values of maximum divergence and convergence are roughly equivalent at this time.

By t = 90 min (Fig. 4.3) west winds of nearly 8 m s^{-1} are occurring 17.5 km ahead of the mesohigh and well to the rear of the wake low. East winds are strongest 20 km ahead of the wake low. West winds now extend 22.5 km to the rear of the mesohigh center,

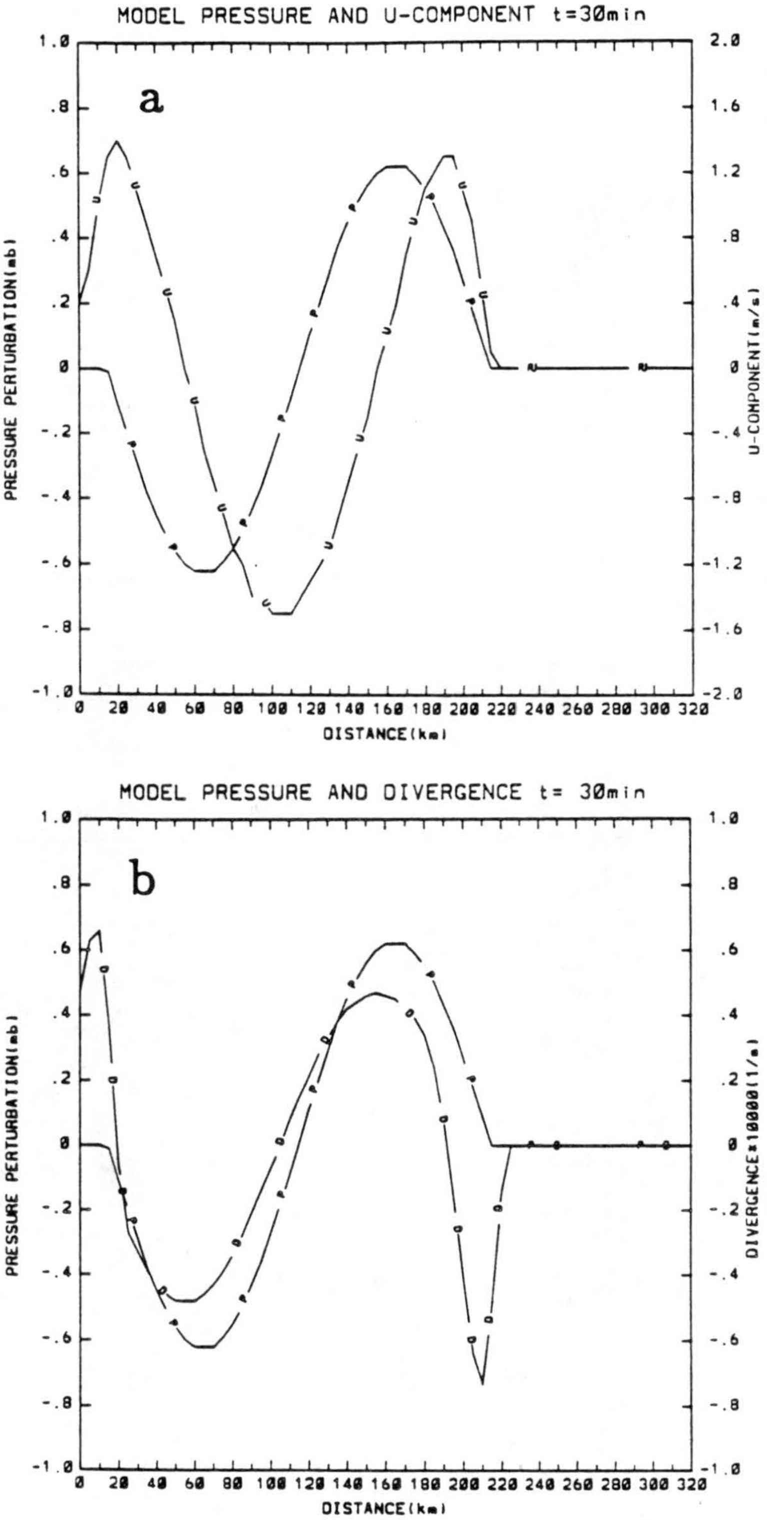

Figure 4.1: Model a.) pressure perturbation (mb) (curve P) and u-component (m s^{-1}) (curve U), and b.) pressure and divergence $\times 10^4$ s^{-1} (curve D) for a pressure wave with a maximum amplitude = 2.5 mb and phase speed = 16.3 m s^{-1}. Model time t = 30 min.

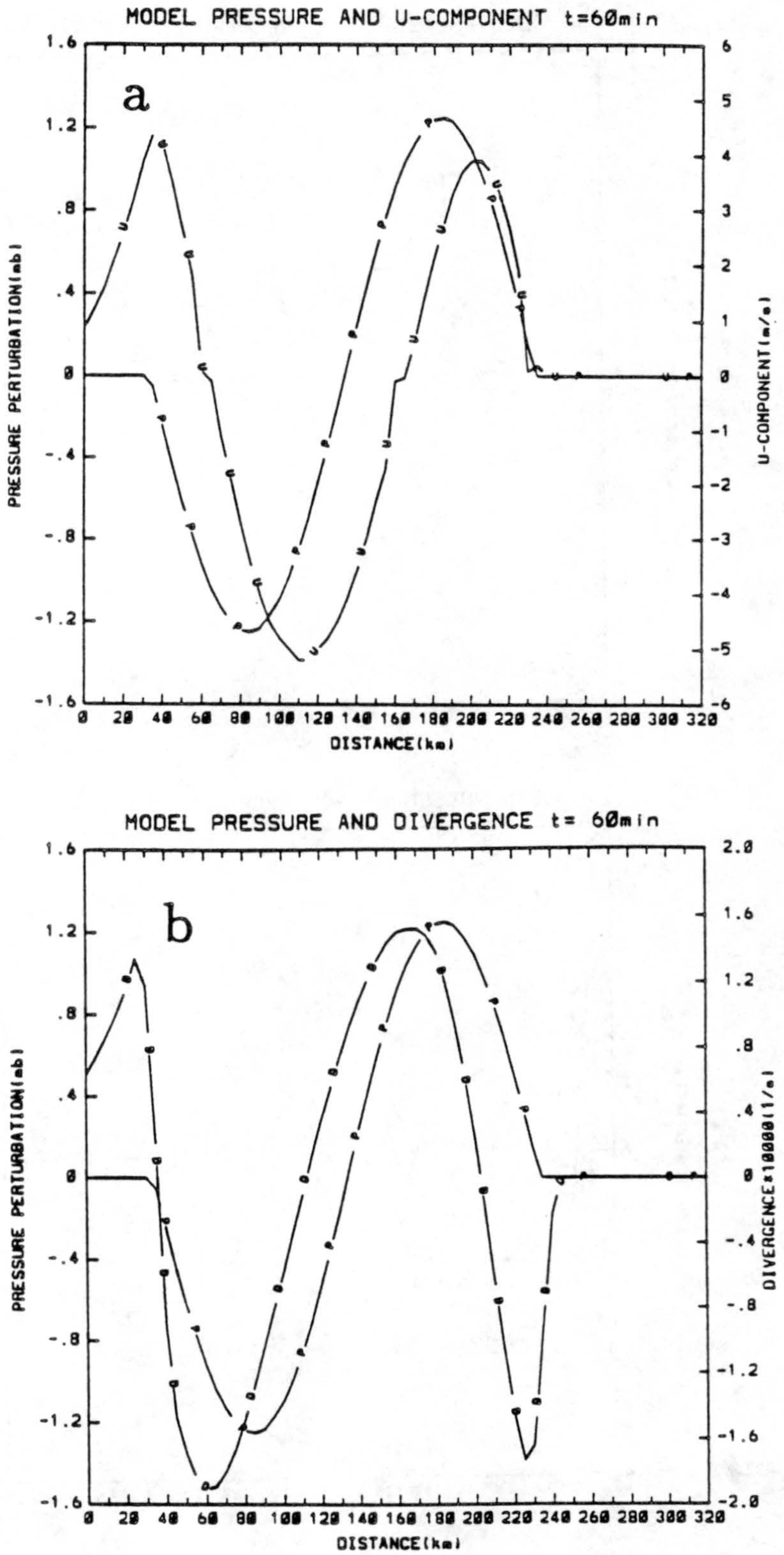

Figure 4.2: Same as Fig. 4.1, except for $t = 60$ min.

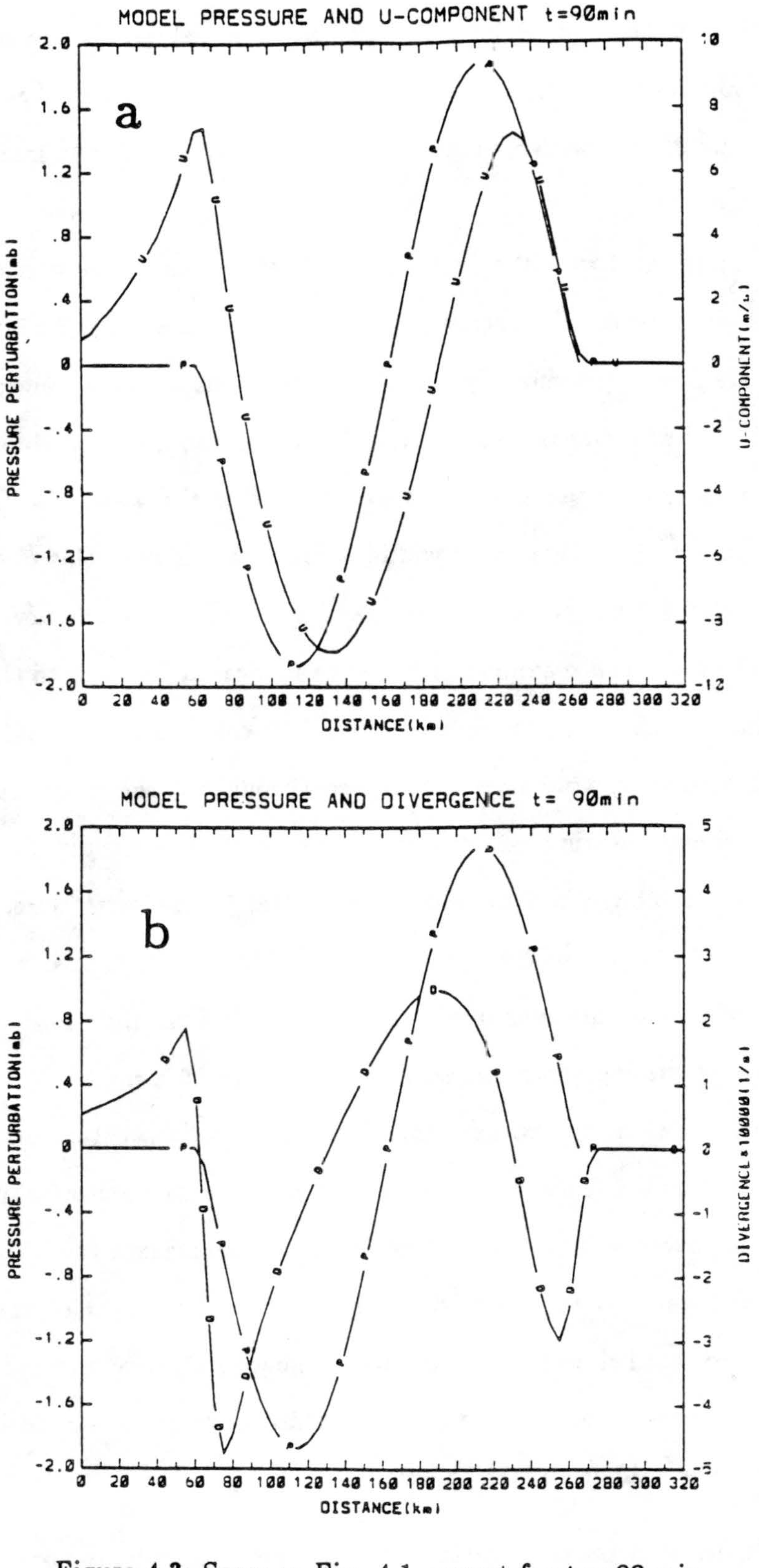

Figure 4.3: Same as Fig. 4.1, except for t = 90 min.

while negative components extend 27.5 km to the rear of the wake low. The maximum divergence to the rear of the mesohigh has increased, and is now located 25 km to the rear of the high center. The convergence to the rear of the wake low has more than doubled in the last 30 min with a maximum value of 4.76×10^{-4} s^{-1} located 37.5 km to the rear of the low center.

Finally, at t = 120 min (Fig. 4.4), the pressure wave has reached its maximum amplitude of 2.5 mb. The strongest westerly winds are found 7.5 km ahead of the mesohigh. They are now approximately the same magnitude as the strongest easterly winds, which are 12.5 km ahead of the wake low. After this time, the west winds ahead of the mesohigh became stronger than the east winds ahead of the wake low (An explanation for the development of stronger west winds is discussed later in this chapter). West winds still extend 22.5 km to the rear of the mesohigh, and east winds now extend 37.5 km behind the wake low. The maximum divergence is located 22.5 km to the rear of the mesohigh, and the maximum convergence is found 47.5 km behind the wake low.

In summary, wind speeds increased throughout the model run as the pressure wave amplified and the wind had time to accelerate. The maximum divergence and convergence increased as the gradient of u-component strengthened with time. West winds were found both ahead of and slightly to the rear of the mesohigh. Likewise, east winds were located ahead of and to the rear of the wake low. The distance that west winds extended to the rear of the mesohigh increased with time to 25 km (or 1/8 of the wavelength of the pressure wave), at t = 90 min, then remained nearly constant until the model offset time at t = 150 min. The east winds, however, extended farther behind the wake low center with each successive timestep. The maximum divergence (convergence) was located near the point where west (east) winds terminated at the rear of the mesohigh (wake low). This is expected since the maximum divergence should occur near the location that winds shift from west to east, while the maximum convergence should be found near the point where winds shift from east to west.

4.2 Comparison of results with different amplitude pressure waves

Table 4.1 displays model results for a 1.5 mb maximum amplitude pressure wave.

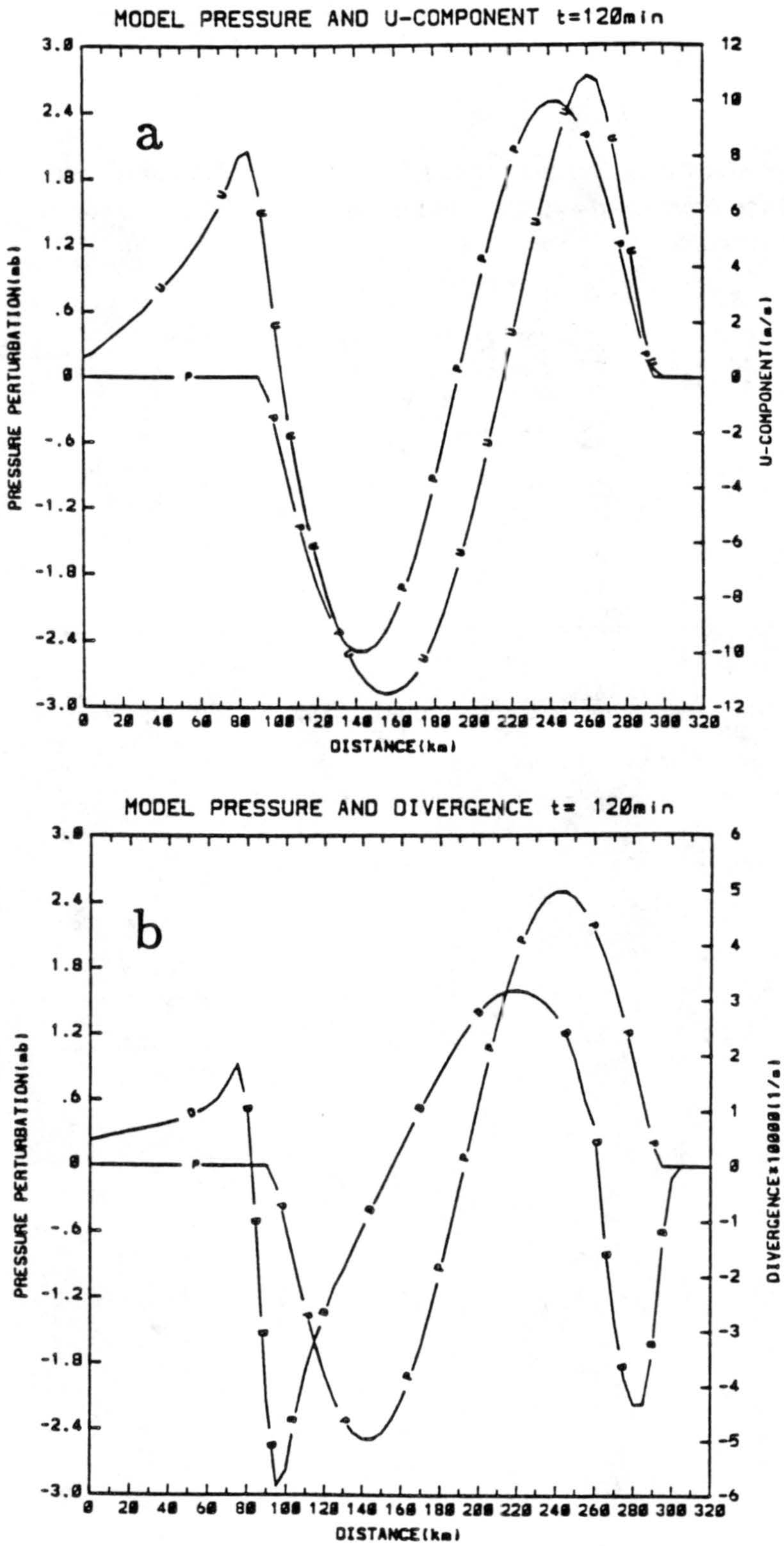

Figure 4.4: Same as Fig. 4.1, except for t = 120 min.

Table 4.1: Model results for the 1.5 mb maximum amplitude pressure wave. "+" indicates that the pressure maximum (minimum) leads the parameter in question, and "-" indicates that it trails.

TIME (MIN)	PRESSURE AMPLITUDE (mb)	MAX WESTERLY COMPONENT (m/s)	MAX EASTERLY COMPONENT (m/s)	MAX DIVG. *10000 (1/s)	MAX CONV. *10000 (1/s)
30	.38	.8	.9	.48	.50
60	.75	2.9	3.3	1.07	1.28
90	1.13	5.6	6.3	1.80	2.78
120	1.50	8.2	8.7	2.46	5.92

SEPARATION(km) OF THE FOLLOWING:

TIME (MIN)	PRESSURE MAX VS. DIV. MAX	PRESSURE MIN VS. CONV. MAX	PRESSURE MAX VS. WESTERLY MAX	PRESSURE MIN VS. EASTERLY MAX
30	+10.0	+10.0	-27.5	-40.0
60	+17.5	+15.0	-22.5	-35.0
90	+17.5	+27.5	-22.5	-25.0
120	+20.0	+40.0	-20.0	-17.5
AVG.	+16.3	+23.1	-23.1	-29.4

The upper portion of this table lists the amplitude, the maximum westerly and easterly component, the maximum divergence, and the maximum convergence associated with the pressure wave at $t = 30$, 60, 90, and 120 min. The lower part of this table lists the various phase shifts discussed in the previous section. At certain times the maximum convergence and divergence in the data field were not associated with the wake low and mesohigh respectively. However, when measuring the phase shift, distances were measured from the center of the mesohigh (wake low) to the local maximum in divergence (convergence) located to the rear of these pressure fields. Table 4.2 and 4.3 are identical to table 4.1, except that they show results for pressure waves with maximum amplitudes of 2.5 and 3.5 mb respectively.

These tables indicate the following trends:

1. The maximum wind speeds (from the east and the west) increase as the phase speed (and hence the maximum amplitude) of the pressure wave increases.

2. The maximum divergence to the rear of the mesohigh follows the same pattern as the wind speed.

3. The maximum convergence to the rear of the wake low increases with pressure wave phase speed through 90 min. At 120 min, this pattern reverses as maximum convergence becomes associated with the 1.5 mb pressure wave.

4. The maximum easterlies are found ahead of the wake low. This maximum shifts closer to the wake low as the phase speed of the pressure wave increases.

5. The maximum westerlies show the same general pattern, expressed in (4) with the mesohigh, but with somewhat greater variability.

6. The separation between the mesohigh and divergence maximum, as well as the wake low and convergence maximum, increase with increasing phase speed.

Table 4.2: Same as Table 4.1, except for the 2.5 mb pressure wave.

TIME (MIN)	PRESSURE AMPLITUDE (mb)	MAX WESTERLY COMPONENT (m/s)	MAX EASTERLY COMPONENT (m/s)	MAX DIVG. *10000 (1/s)	MAX CONV. *10000 (1/s)
30	.62	1.3	1.5	.47	.73
60	1.25	4.4	5.2	1.52	1.91
90	1.87	7.2	8.9	2.47	4.76
120	2.50	10.9	11.5	3.18	5.76

SEPARATION(km) OF THE FOLLOWING:

TIME (MIN)	PRESSURE DIV. VS. MAX MAX	PRESSURE CONV. VS. MIN MAX	PRESSURE WESTERLY VS. MAX MAX	PRESSURE EASTERLY VS. MIN MAX
30	+10.0	+10.0	-27.5	-40.0
60	+17.5	+25.0	-17.5	-27.5
90	+25.0	+37.5	-17.5	-20.0
120	+22.5	+47.5	-17.5	-17.5
AVG.	+18.8	+30.0	-20.0	-26.3

Table 4.3: Same as Table 4.1, except for the 3.5 mb pressure wave.

TIME (MIN)	PRESSURE AMPLITUDE (mb)	MAX WESTERLY COMPONENT (m/s)	MAX EASTERLY COMPONENT (m/s)	MAX DIVG. *10000 (1/s)	MAX CONV. *10000 (1/s)
30	.88	1.9	2.1	.81	.92
60	1.75	5.6	6.8	1.98	2.66
90	2.27	9.1	10.8	2.96	5.72
120	3.50	13.6	13.5	3.84	5.36

SEPARATION(km) OF THE FOLLOWING:

TIME (MIN)	PRESSURE MAX VS. DIV. MAX	PRESSURE MIN VS. CONV. MAX	PRESSURE MAX VS. WESTERLY MAX	PRESSURE MIN VS. EASTERLY MAX
30	+7.5	+10.0	-27.5	-40.0
60	+20.0	+30.0	-17.5	-25.0
90	+25.0	+40.0	-15.0	-12.5
120	+25.0	+45.0	-20.0	-10.0
AVG.	+19.4	+31.3	-20.0	-21.9

4.3 Explanation of trends

In this section a possible explanation for each of the trends is presented. A program has been developed to track an air parcel through the mesoscale pressure waves used in the model. Air parcel trajectories are used to help explain the variability in the wind and divergence fields that arise when using different amplitude pressure waves.

First, trend 1 is explainable since the amplitude of the pressure wave increases with increasing phase speed. A higher amplitude produces a stronger pressure gradient, which increases the wind speed. Although the maximum wind speeds are greater with a higher amplitude pressure wave, they are not as great as one might first expect. For example, at $t = 120$ min (refer to tables 4.2 and 4.3), the maximum easterly component with the 3.5 mb wave is only 2 m s^{-1} greater than that associated with the 2.5 mb (16.3 m s^{-1}) wave. The reason for only a slight increase in wind speed is due to the higher phase speed (19.3 m s^{-1}) of the 3.5 mb wave. Air parcels were tracked through these two pressure waves from the mesohigh center at $t = 10$ min, until they reached the center of the wake low. In this region $\frac{\partial p}{\partial x}$ is positive and is therefore a favorable region for air parcels to accelerate towards the west. Both parcels initially had zero velocity. In the case of the 16.3 m s^{-1} wave, the parcel had a residence time of 84 min in the favorable pressure gradient. Upon exiting this gradient, the parcel had attained a speed of -8.3 m s^{-1} (negative implies from the east). The parcel moved through the same region of the 19.3 m s^{-1} wave in only 72 min, attaining a speed of -8.6 m s^{-1}. This information shows that the higher amplitude wave caused the parcel to obtain a higher speed. However, the parcel was located in a region favorable for acceleration for a shorter period of time. Therefore, the parcel speed in the 3.5 mb wave was only *slightly* greater than that in the 2.5 mb wave.

Trends 2 and 3 state that the divergence and convergence fields follow the same pattern (except for the convergence at 120 min which will be addressed separately) as the wind speed. This observation makes physical sense. As the maximum wind speeds increase, the wind speed gradient strengthens. A stronger wind speed gradient will increase the divergence and convergence.

The reversal in the convergence maximum, explained in trend 3, is a result of the relatively strong west winds that build up near the back edge of the wake low associated with the 1.5 mb pressure wave. Figure 4.5 shows that, for this wave, west winds are reaching 8 m s^{-1} near the back edge of the wake low, while Fig. 4.6 indicates that the highest westerly wind to the rear of the wake low, in the 3.5 mb wave, is only 7.4 m s^{-1}. The slightly higher wind velocity to the rear of the wake low, in the 1.5 mb wave, produces a wind speed gradient that locally exceeds the maximum gradient found at the rear of the low in the 3.5 mb wave. This produces slightly higher maximum convergence values.

To explain the stronger west winds near the back edge of the wake low in the lower amplitude wave, air parcels were followed through each wave from the center of the wake low, at $t = 60$ min, until the parcel reached the flat pressure gradient 50 km to the rear. In this region, $\frac{\partial p}{\partial x}$ is negative, and is therefore a favorable region for an eastward acceleration of parcels. The initial parcel speeds were -1.6 and -5.0 m s^{-1} in the 1.5 and 3.5 mb pressure waves respectively. The parcel in the 1.5 mb wave had a residence time of 84 min, and reached a speed of 7.4 m s^{-1} upon exiting the wave. The parcel in the 3.5 mb wave had a residence time of only 41 min, and reached a speed of only 5.4 m s^{-1}. Therefore, it can be concluded that the slower movement of the pressure wave allowed for a higher parcel residence time in a region favorable for an eastward acceleration. The higher residence time allowed stronger west winds in this wave, despite the much lower pressure amplitude.

Trends 4 and 5 state that maximum easterlies (westerlies) are found ahead of the wake low (mesohigh) rather than right near the pressure centers. At first glance this result may seem somewhat surprising. Normally, one would expect to see the strongest winds right near the low center. This is not the case, however, because the pressure wave is amplifying with time. Two air parcels in the (19.3 m s^{-1}) wave were started at the mesohigh, one at $t = 20$ min, and the other at $t = 30$ min. The first parcel reached the wake low after 70 min, or at $t = 90$ min, with a speed of -9.7 m s^{-1}. At this time, the second parcel was located 17.4 km ahead of the wake low and had a speed of -10.7 m s^{-1}. It later reached a maximum speed of 11.2 m s^{-1} once within 2 km of the wake low. The second parcel was able to attain a higher speed than the first, even though it was located well to the east

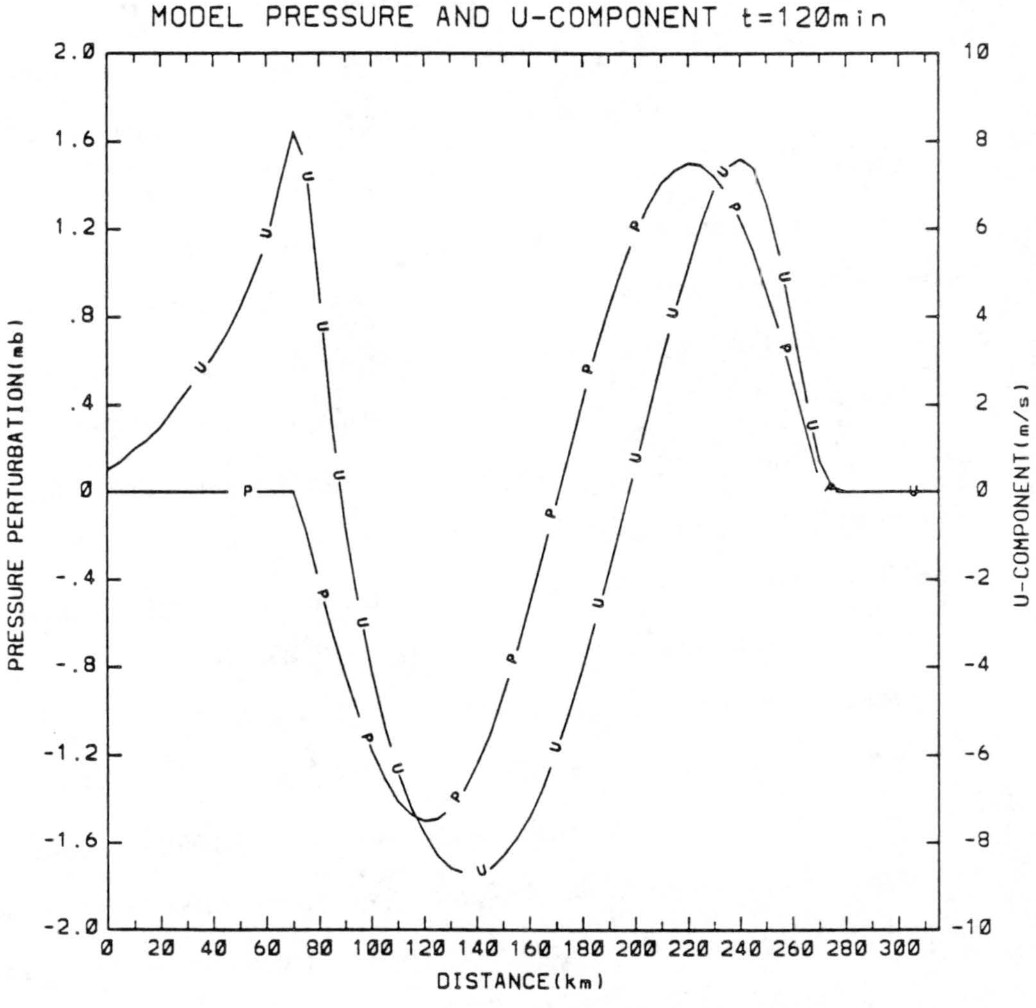

Figure 4.5: Model pressure perturbation and u-component for a pressure wave with a maximum amplitude = 1.5 mb and phase speed = 12.6 m s^{-1}. Model time t = 120 min.

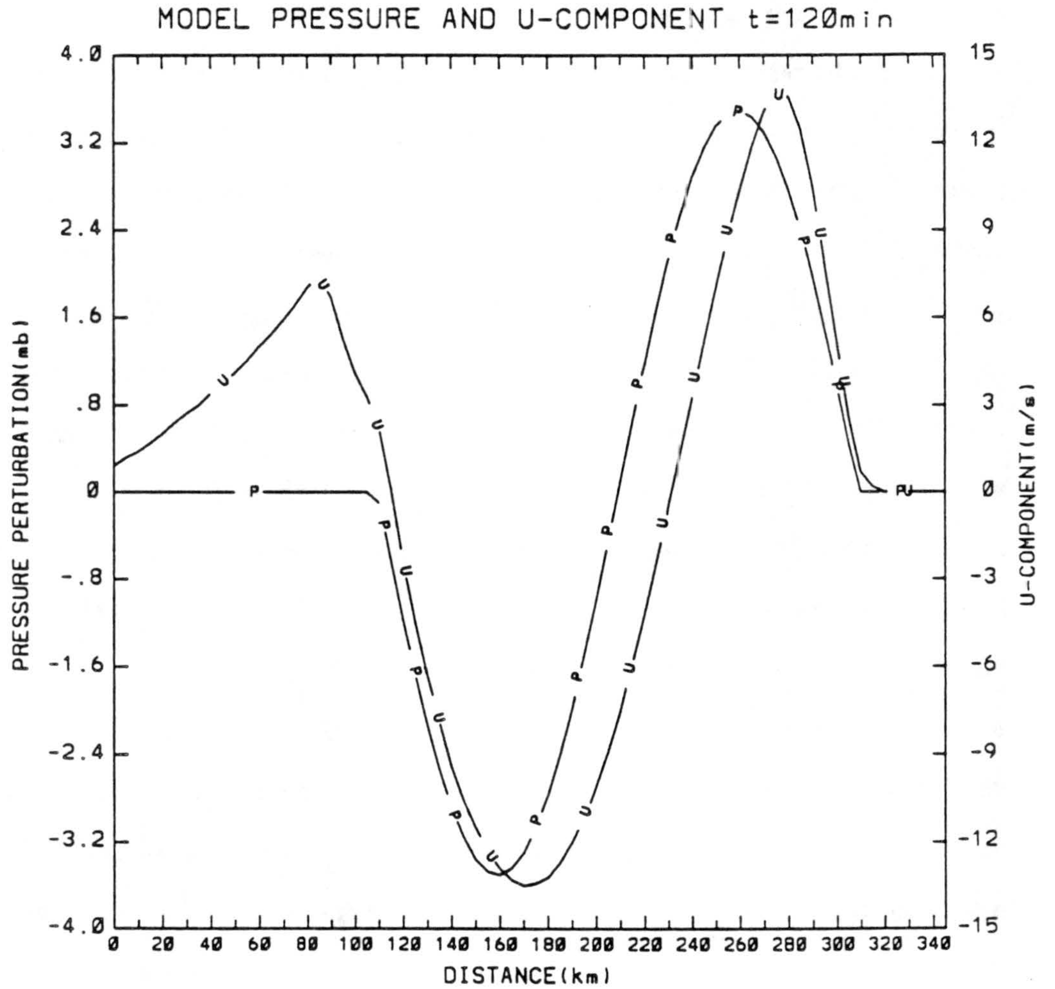

Figure 4.6: Same as Fig. 4.5, except for a pressure wave with a maximum amplitude of 3.5 mb and phase speed = 19.3 m s^{-1}.

of the wake low. This was possible because the pressure wave had amplified by the time the second parcel entered the region between the mesohigh and wake low. The stronger pressure gradient created by this amplification allowed for a more rapid acceleration of the air parcel to the west.[5] Figure 4.7 displays the pressure and wind field for this wave at $t = 90$ min. The maximum wind from the east is 10.8 m s^{-1} and is located 12.5 km ahead of the wake low.

Trends 4 and 5 also indicate that the location of maximum easterlies (westerlies) shift closer to the wake low (mesohigh) as the phase speed of the pressure wave increases. The reason for this is not obvious. However, this shift is probably related to the higher speed of the wave, rather than the higher amplitude.

The model results show that the convergence (divergence) maximum is located farther to the rear of the wake low (mesohigh) as the phase speed of the pressure wave increases (trend 6). This observation is easily explained. An air parcel, whose original location is ahead of the mesohigh, will experience an eastward acceleration. However, the pressure wave is moving to the east faster than the air parcel, so effectively the air parcel is moving to the west relative to the pressure wave. Eventually, the parcel will cross the center of the mesohigh, even though it is moving towards the east (*i.e.* a west wind), and be located in a region where $\frac{\partial p}{\partial x}$ is positive. At this point, the parcel will slow down, reverse its direction, and head towards the west. This procedure takes time, during which the mesohigh has moved downstream. This explains the westerly winds to the rear of the mesohigh. The distance that these west winds extend behind the mesohigh is related to the mesohigh's phase speed. If the mesohigh is moving rapidly, it will have moved a considerable distance before the air parcel reverses its direction. Therefore, the distance, that west winds extend to the rear of the mesohigh, is proportional to the high's phase speed. The above scenario is true for the east winds extending to the rear of the wake low, except that the distance is increased because parcels passing through the center of the wake low are moving in the opposite direction of pressure wave motion.

---

[5]The same argument presented here applies to the maximum westerly winds ahead of the mesohigh.

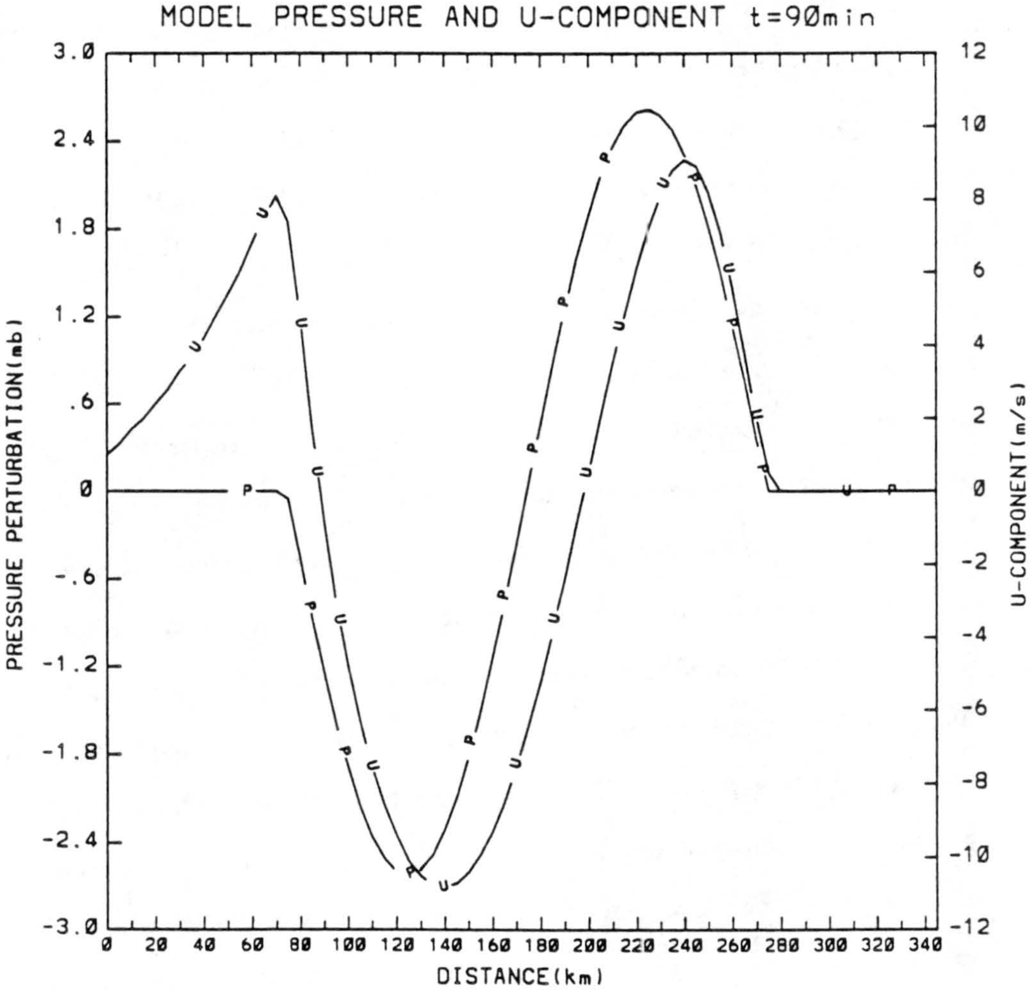

Figure 4.7: Same as Fig. 4.6, except for t = 90 min.

One final point, which was mentioned in section 4.1, deserves some attention. It was stated that, after $t = 120$ min, the maximum westerlies ahead of the mesohigh exceeded the maximum easterlies ahead of the wake low. Figure 4.8 is a plot of pressure and u-component at $t = 150$ min for the 16.3 m s^{-1} pressure wave. At this time, maximum westerlies of nearly 15 m s^{-1} are occurring ahead of the mesohigh. The maximum easterlies ahead of the wake low are only 12 m s^{-1}. The build up of the westerly winds, beyond the strength of the easterly winds, can, once again, be explained by parcel trajectories. Two air parcels were followed through the 16.3 m s^{-1} wave beginning at $t = 70\,min$. The first parcel began at the leading edge of the pressure wave (50 km ahead of the mesohigh center), and the second at the center of the mesohigh. At model offset time ($t = 150$ min), the first parcel had attained a speed of 13.5 m s^{-1} at a location 11 km ahead of the mesohigh. Therefore, in 80 min, the parcel was displaced (the word displaced is preferred rather than moved since the pressure wave is moving as well) only 39 km. The second parcel, on the other hand, had a speed of -12.6 m s^{-1} (again negative implies motion from the east) at a location of 5 km ahead of the wake low. Therefore, this parcel was displaced 95 km in the same amount of time, and was about to exit the region favorable for a westward acceleration (*i.e.* the parcel would soon decelerate). This explains why the maximum westerlies eventually exceed the maximum easterlies. Parcels located ahead of the mesohigh are moving in the same direction as the pressure wave. This allows these parcels to remain in a region favorable for continued acceleration longer than those located to the rear of the mesohigh. The latter are moving in the opposite direction of the wave, and therefore spend less time in a region favorable for acceleration. This effect is not noticed until late in the model run because the pressure gradient, ahead of the mesohigh, has to be sufficiently strong to allow parcels to gain enough momentum to remain ahead of the high center. It appears that the maximum westerly wind is limited by the phase speed of the pressure wave. As the speed of an air parcel begins to exceed the phase speed of the pressure wave, the parcel will eventually outrun the wave. The parcel will then encounter the flat pressure gradient ahead of the mesohigh, and decelerate. This type of parcel movement might explain the surging motion of many gust fronts.

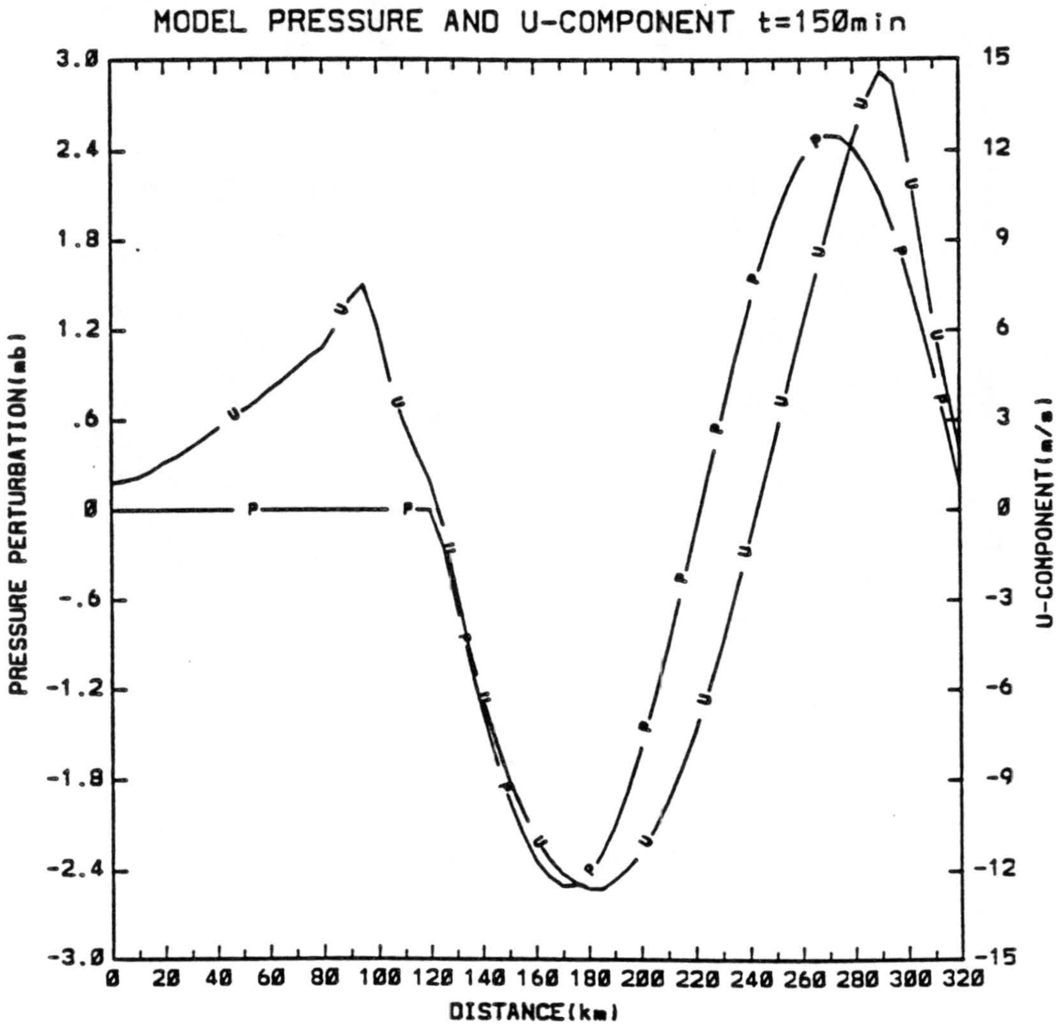

Figure 4.8: Model pressure and u-component for a pressure wave with a maximum amplitude of 2.5 mb and a phase speed of 16.3 m s^{-1}. Model time $t = 150$ min.

Chapter 5

DATA SET AND ANALYSIS PROCEDURE

5.1 PRE-STORM

The O-K PRE-STORM (Oklahoma-Kansas Preliminary Regional Experiment for STORM CENTRAL) project was conducted in May and June of 1985 to study the development, evolution, and structure of MCS's that frequently affect the Great Plains during the summer. A dense network of ground-based automated stations approximately 50 km apart was used to study the surface features associated with these systems. The northern part of the mesonetwork consisted of 40 NCAR[6] PAM (Portable Automated Mesonetwork) stations, while the southern half consisted of 42 NSSL[7] SAM (Surface Automated Mesonetwork) stations. Two additional PAM stations were collocated with two of the SAM stations for the purpose of comparison. Both the PAM and SAM stations collected data every 5 min. In addition, there was extensive radar and upper-air coverage over the two state area. Figure 5.1 displays the location of the mesonetwork, radar, rawindsonde, and profiler sites, while Fig. 5.2 shows the surface mesonetwork in greater detail including the identifier for each site.

5.2 Treatment of the surface data

5.2.1 Pressure reduction

Since large errors can occur when reducing pressure to sea level, pressures at the PAM/SAM stations were reduced to 518 m (after Johnson and Hamilton, 1988), which

[6]NCAR: National Center for Atmospheric Research

[7]NSSL: National Severe Storms Laboratory

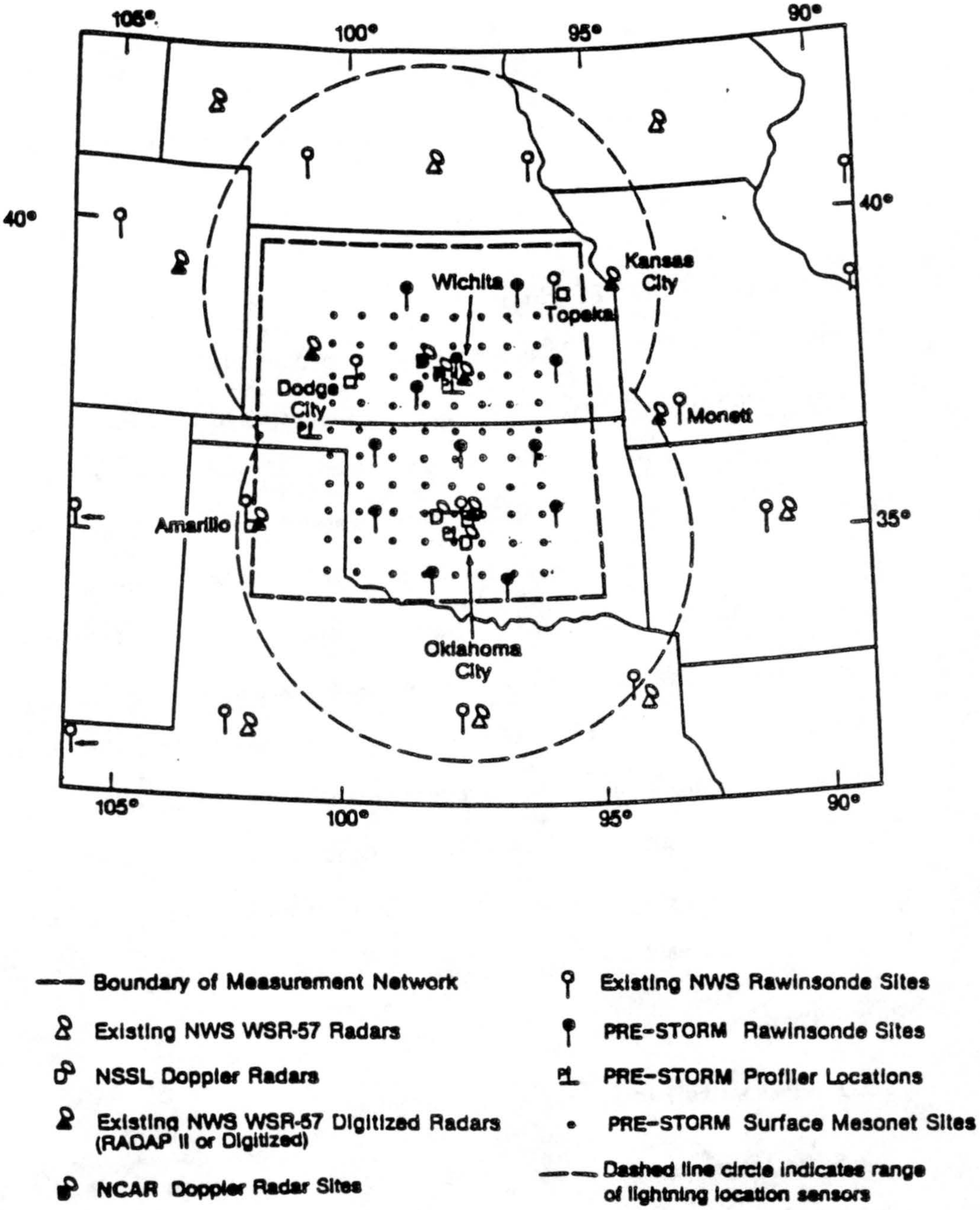

Figure 5.1: The OK PRE-STORM observational mesonetwork (from Cunning, 1986).

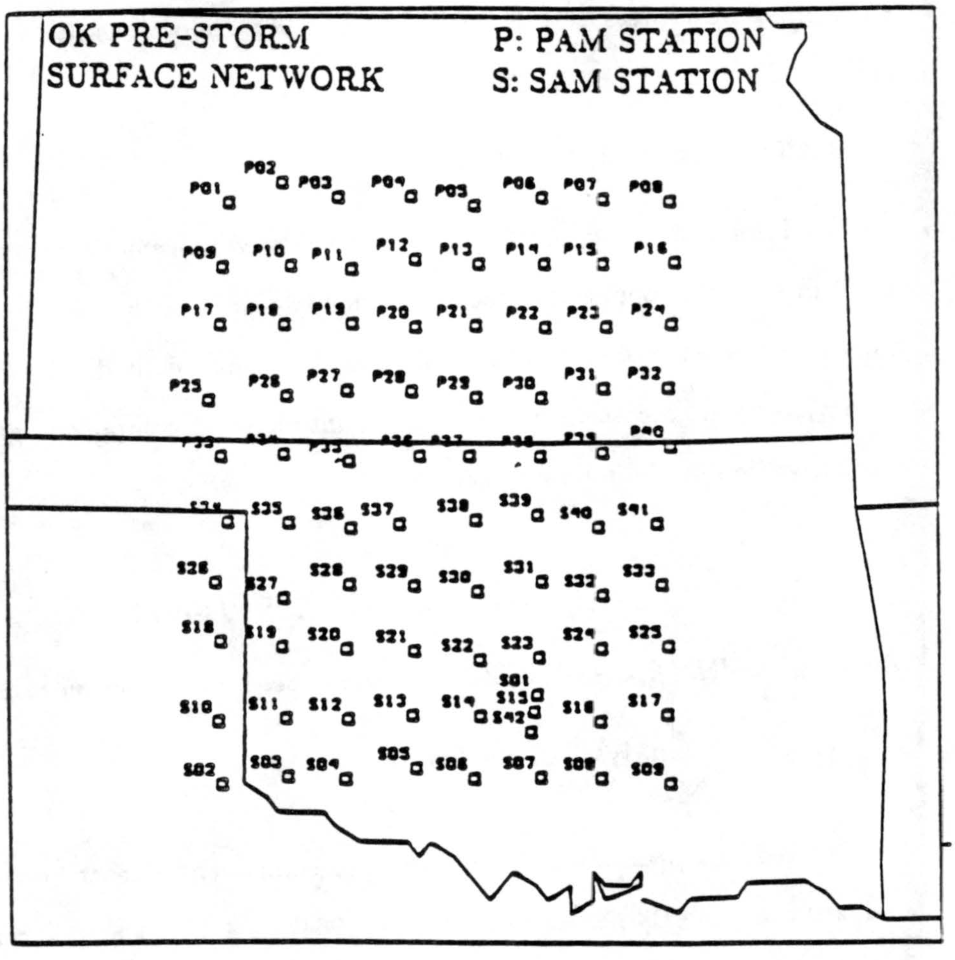

Figure 5.2: The PRE-STORM Portable Automated Mesonetwork (PAM) and Surface Automated Mesonetwork (SAM) grid.

is the average height of the PAM stations. To obtain the reduced pressure the following equation was used:

$$P_{518m} = p_{sta} exp\left[\frac{g(518 - z_{sta})}{R_d \bar{T}_v}\right] , \tag{5.1}$$

where p_{sta} and z_{sta} are the station's pressure and elevation in meters respectively. Gravity $g = 9.8$ m s^{-2} and the gas constant for dry air $R_d = 287$ J kg^{-1} K^{-1}. T_v, the mean virtual temperature, is approximated by the surface virtual temperature. Once the reduced pressure was calculated at each station, corrections were applied to remove the diurnal and semi-diurnal pressure tides (see Stumpf, 1988), as well as the measurement biases of individual stations.

5.2.2 Treatment of the wind field

Isochrones of the squall line gust front show a movement from approximately 310° at 16 m s^{-1} (this applies for the southern two-thirds of the gust front. The gust front moved somewhat more slowly in Kansas). This analysis is displayed in Fig. 5.3. The wind velocity at a station was translated into a wind component perpendicular to the convective line by the following equation:

$$u_{\perp} = u_{sta} cos(310° - DIR_{sta}) , \tag{5.2}$$

where u_{sta} and DIR_{sta} are the station's wind speed and direction respectively.

5.3 Objective analysis procedure

The reduced pressure and perpendicular component at each station was objectively analyzed using the Barnes scheme (Barnes, 1964). A 4.5° × 4.5° grid centered on 36.75°N and 98.25°W was used with a grid spacing of 20 km. Once these fields were objectively analyzed, true u and v components were calculated from $u_{\perp}$ at each gridpoint, after which the horizontal divergence ($\frac{\partial u}{\partial x} + \frac{\partial v}{\partial y}$) was computed.

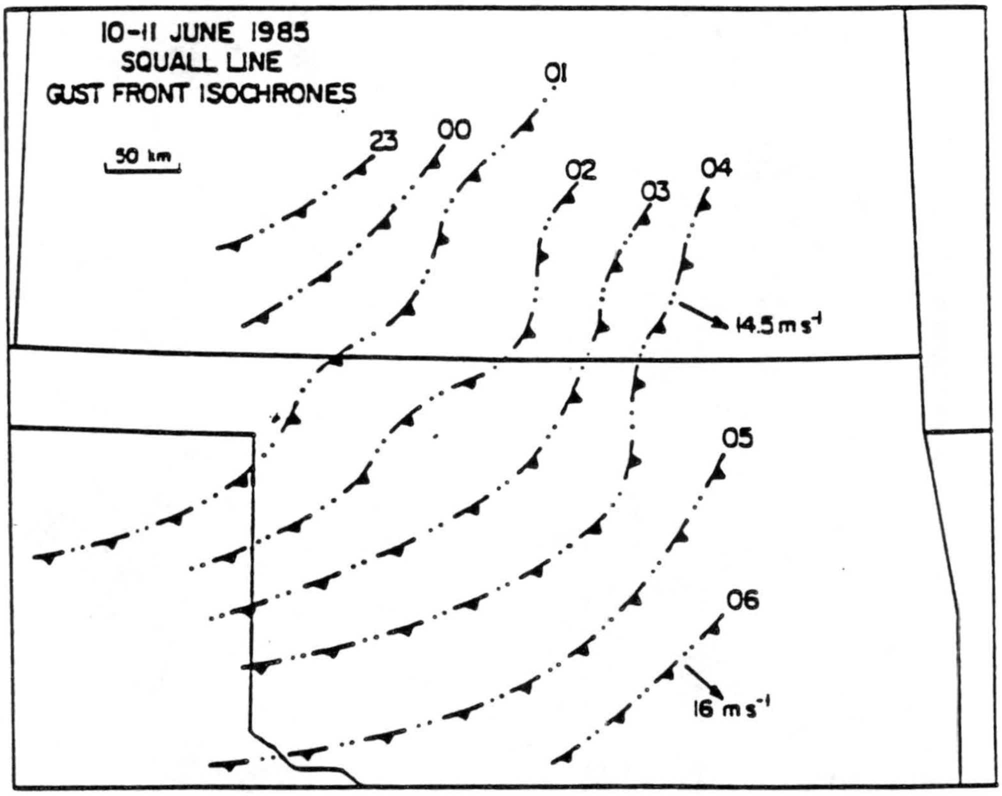

Figure 5.3: Squall-line gust front isochrones for 10–11 June 1985 (from Johnson and Hamilton, 1988).

Chapter 6

OBSERVATIONS OF THE 10–11 JUNE MCS

The MCS of 10–11 June, 1985 was the most intense and widely studied convective system in **PRE-STORM**. Johnson and Hamilton (1988) discussed in detail the life cycle of this MCS as it moved southeast at from western Kansas late on the 10th, to south-central Oklahoma early on the 11th. Smull and Houze (1987) studied the structure of this MCS using single Doppler data, while Rutledge *et al.* (1988) studied this MCS using single Doppler data, as well as, conventional radar and satellite imagery. Finally, Zhang *et al.* (1989) numerically simulated this MCS using a nested-grid model.

In this chapter, attention is focused on the surface mesoscale pressure fields (hereafter referred to as MPF's) associated with this MCS, and the wind's response to these features. Of particular interest is the time period from 0100–0400 UTC on the 11th, during which the MCS, as well as the mesoscale pressure fields, reached their peak intensity. Model results will be compared to the observed wind field in the next chapter.

6.1 Mesoscale pressure fields

Figures 6.1–6.4 display surface pressure, reduced to 518 m, in one hour intervals from 0100 to 0400 (all times are UTC unless otherwise noted) on the 11th. Figure 6.1 clearly displays a strong mesohigh located over southwest Kansas at 0100. The maximum surface pressure in the high was 954 mb. Ahead of the mesohigh, was a pre-squall mesolow. Notice that a weak area of low pressure (denoted by the 949 mb contour) was beginning to develop to the rear of the mesohigh. By 0200 (actually as early as 0130) (Fig. 6.2) , this feature became the wake low as a closed low pressure circulation developed northwest of the mesohigh. The sequence of events where the wake low formed well after the appearance of the mesohigh, is consistent with the findings of Johnson and Hamilton (1988).

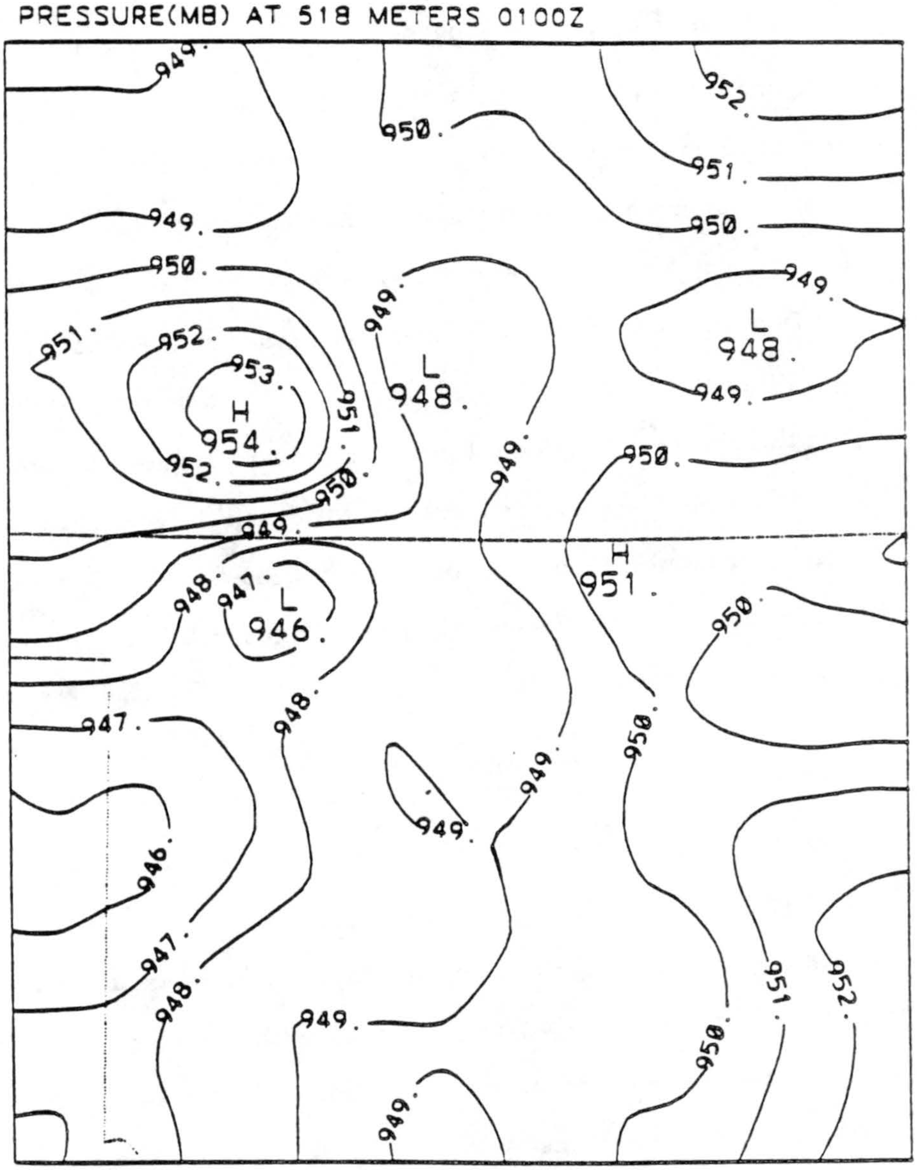

Figure 6.1: Objectively analyzed pressure (mb), reduced to 518 m, at t = 0100 UTC on the 11th.

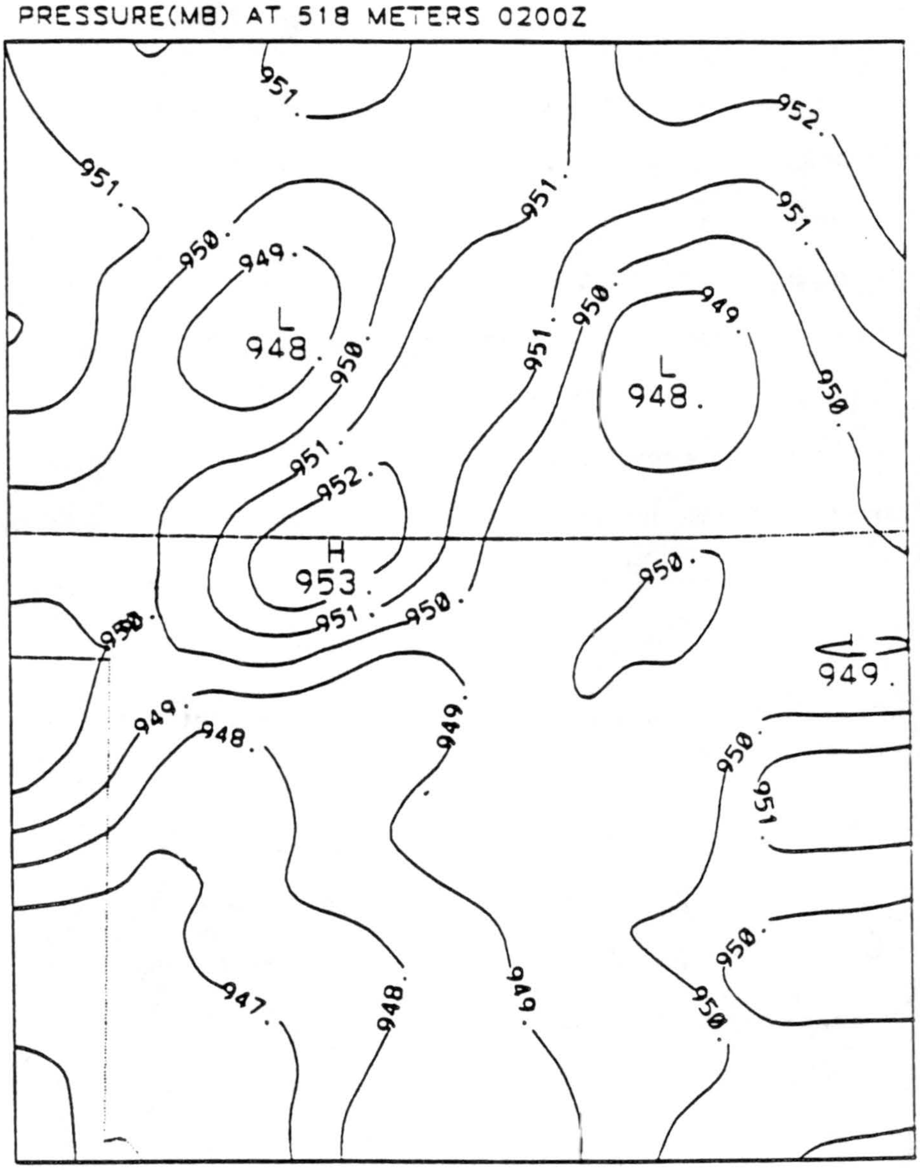

Figure 6.2: Same as Fig. 6.1, except for 0200 UTC.

Figure 6.2 also indicates that the mesohigh moved southeast and weakened slightly as maximum pressures decreased to 953 mb. Figure 6.3 shows that, by 0300, which is when the MCS reached its peak intensity, the wake low was very extensive with a major axis of approximately 200 km. Johnson and Hamilton (1988) point out that between 0100-0300, the stratiform region intensified and became more widespread. This may account for the rapid development and increased areal coverage of the wake low during this period. By 0300, the maximum pressure in the mesohigh had increased to 954 mb as it continued its southward trek into north-central Oklahoma. Finally, by 0400 (fig. 6.4) , the mesohigh, now well into Oklahoma, had shown a slight intensification as the maximum central pressure had risen to 955 mb. The wake low had diminished somewhat, both in areal coverage and intensity, as it drifted eastward.

Figure 6.5 summarizes the track of the mesohigh and wake low during the time period of interest. The mesohigh moved southeast with the leading convective line from southwest Kansas at 0100 to south-central Oklahoma by 0400. The wake low, on the other hand, moved in a more east-southeast direction. This indicates that these two features moved independently. The movement of the mesohigh is dictated by the movement of the convective line, while the movement of the wake low is most likely controlled by the interaction of the rear-inflow jet with the stratiform rain area.

6.2 Wind flow and divergence patterns associated with the mesoscale pressure fields

Figures 6.6-6.9 display the wind flow and divergence patterns associated with the MPF's discussed in the previous section. Each figure has 3 parts: (*a*) is, once again, the pressure reduced to 518 m, (*b*) is the wind component normal to the convective line, and (*c*) is the divergence field multiplied by 10^4.

To begin with, at 0100 (Fig. 6.6), maximum positive normal wind components (hereafter referred to as maximum positive components) of approximately 10 m s^{-1} were found just south of the mesohigh center. Positive components extended to back edge of the mesohigh axis, indicating that the instantaneous airflow was directed *forward* through this pressure field. A small area of negative components was located well to the rear of

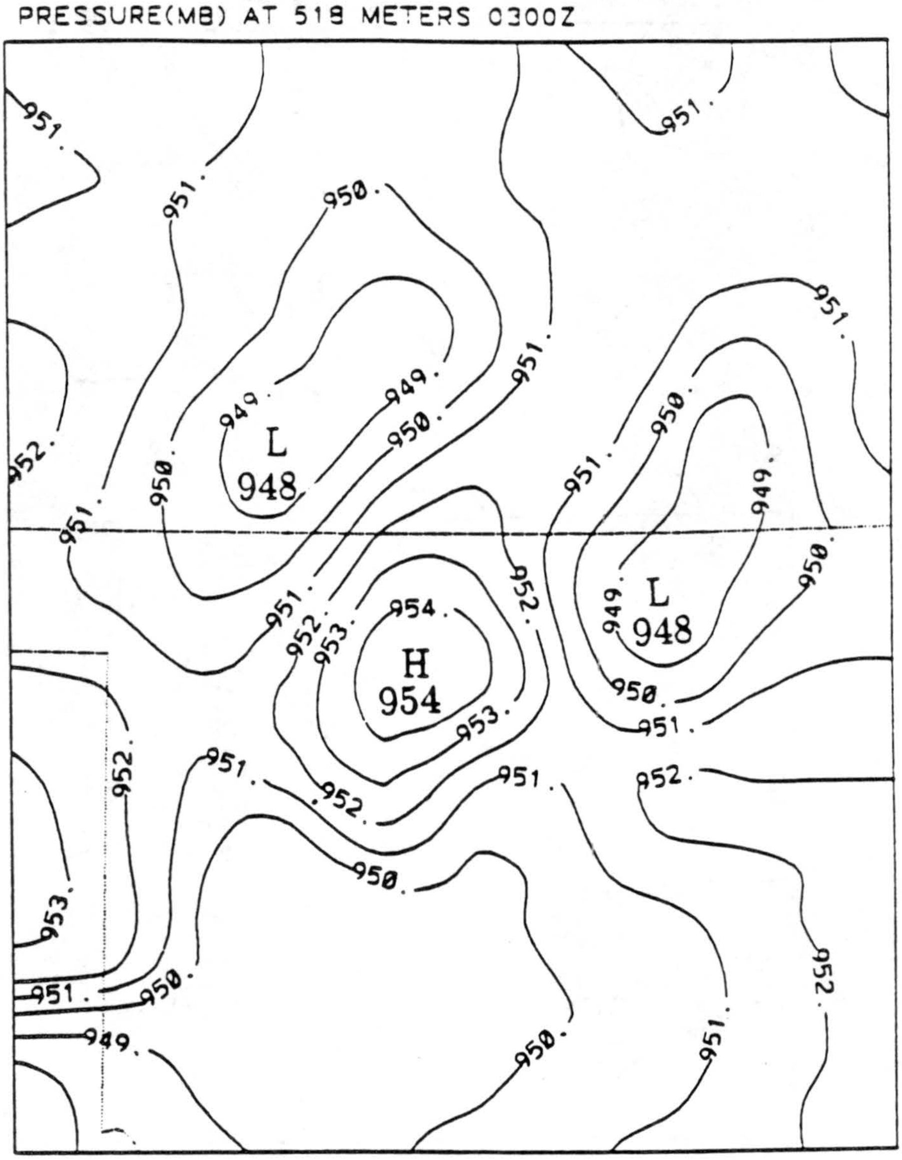

Figure 6.3: Same as Fig. 6.1, except for 0300 UTC.

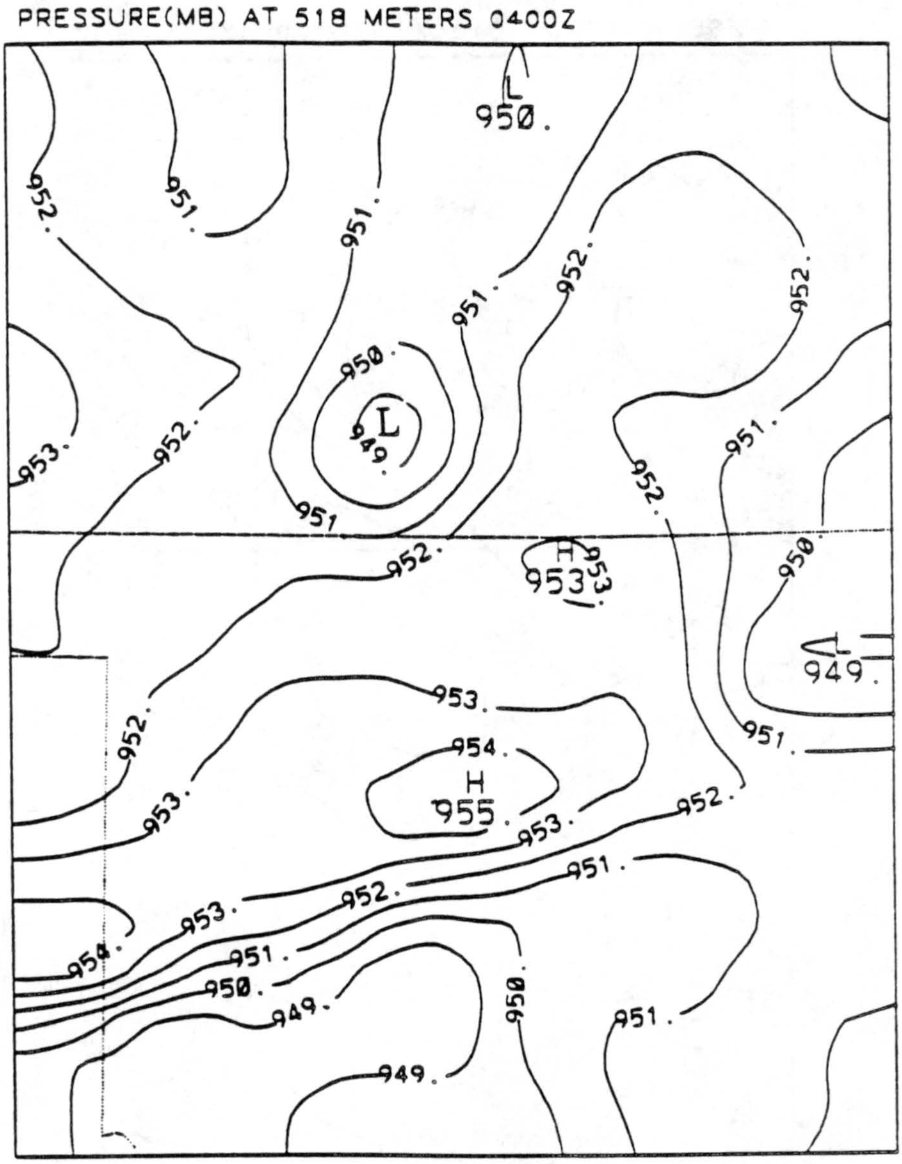

Figure 6.4: Same as Fig. 6.1, except for 0400 UTC.

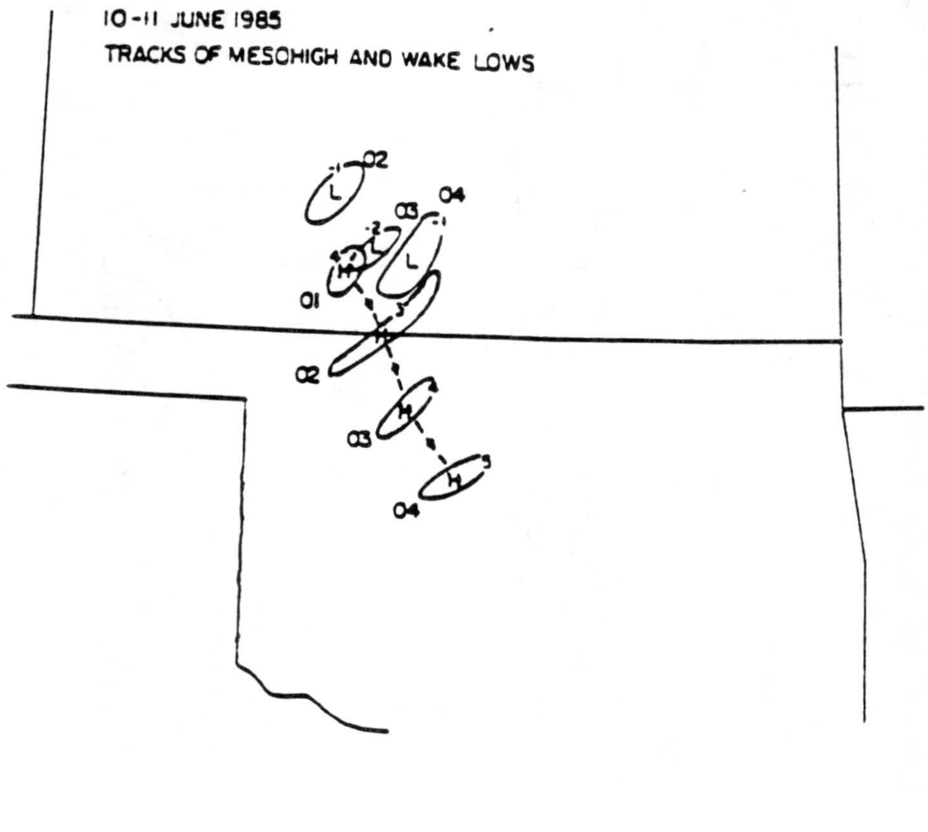

Figure 6.5: Tracks of mesohigh and wake low from 0100-0400 UTC on the 11th. Innermost closed isobars are drawn and labeled as departures from 950 mb (modified from Johnson and Hamilton, 1988).

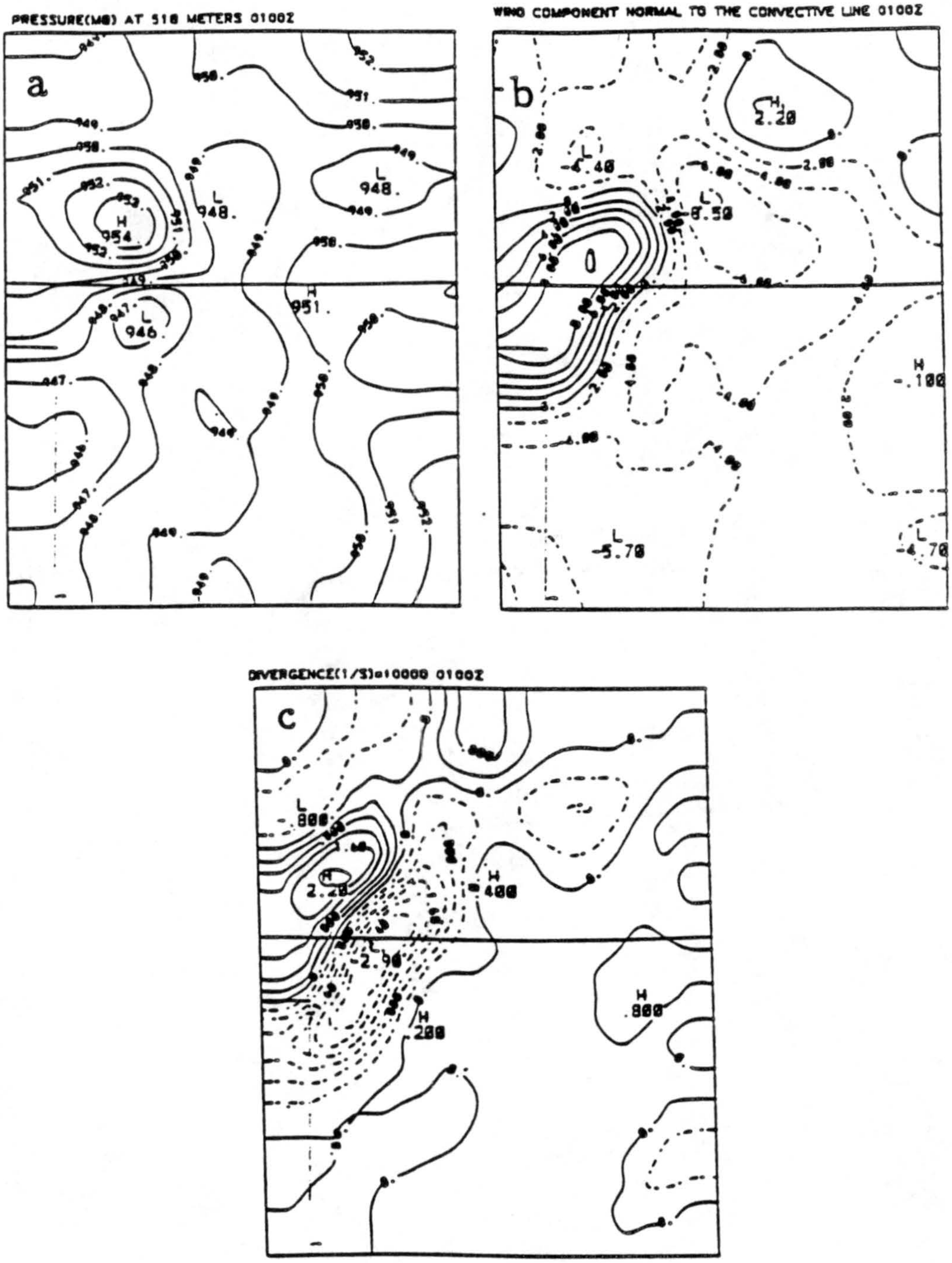

Figure 6.6: Objective analysis of a.) pressure (mb), reduced to 518 m, b.) wind component (m s^{-1}) normal to the convective line, and c.) divergence $\times 10^4$ s^{-1} at 0100 UTC on the 11th.

the mesohigh in association with the developing wake low. The divergence field shows that the maximum divergence was occurring several km to the rear of the mesohigh axis. Strong convergence began just ahead of the mesohigh and extended approximately 100 km downstream. This region of convergence was associated with the thunderstorm gust front emanating from the mesohigh. Finally, an area of weak convergence was located near the developing wake low.

Figure 6.7 shows that, at 0200, a similar pattern in both the wind and divergence fields existed. Maximum positive components of about 8 m s^{-1} were found just ahead of the mesohigh, particularly to the northeast along the ridge axis extending into south-central Kansas. The lower wind maximum may be due to the slight weakening of the mesohigh during this time period. Again, the positive components to the rear of the mesohigh reflect a forward air flow through this feature. By this time, the wake low had become fully developed and maximum negative components were occurring just east of the low center. Negative components extend to the back edge of the wake low suggesting that the instantaneous airflow was directed *rearward* through this pressure feature. The divergence field associated with the mesohigh is also similar to that in Fig. 6.6, except that the magnitude of maximum divergence and convergence decreased slightly, which can be attributed to the lighter winds associated with the weaker mesohigh. At this time, an area of convergence was located at the rear of the wake low. The magnitude of this convergence was about one-half the magnitude of that occurring ahead of the mesohigh along the gust front.

At 0300 (Fig. 6.8), the mesohigh had strengthened slightly to a maximum central pressure of 954 mb. The wind field responded with maximum positive components reaching 13.4 m s^{-1} just ahead of the high center. A secondary maximum of 8.2 m s^{-1} was occurring northeast of the mesohigh ahead of the weak pressure ridge. As in the previous time periods, positive wind components extended to the rear of the mesohigh. The negative components just ahead of the wake low increased to 7.3 m s^{-1} as the wake low reached its maximum areal extent. Negative components again extended to the back edge of the wake low. The divergence to the rear, and the convergence ahead, of the mesohigh increased

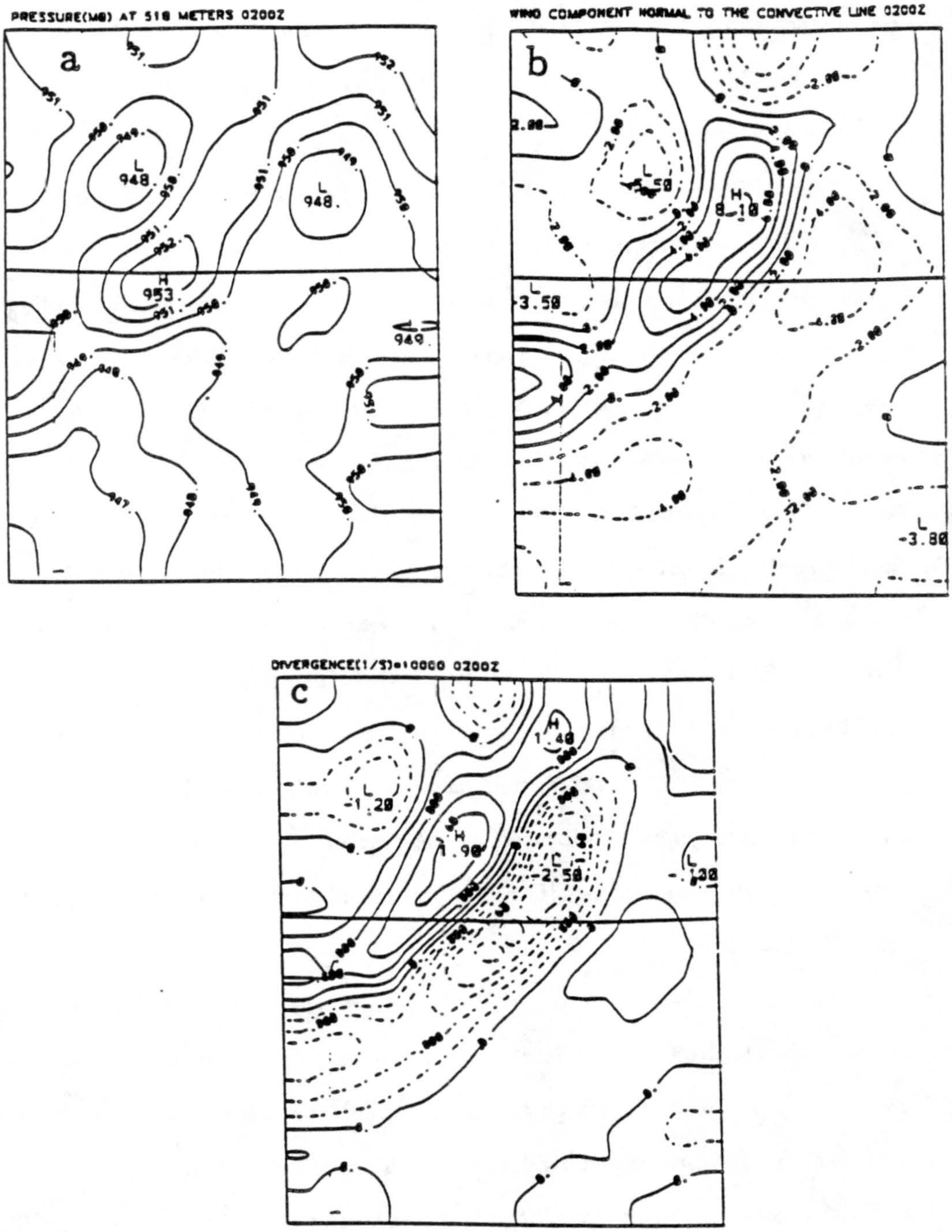

Figure 6.7: Same as Fig. 6.6, except for 0200 UTC.

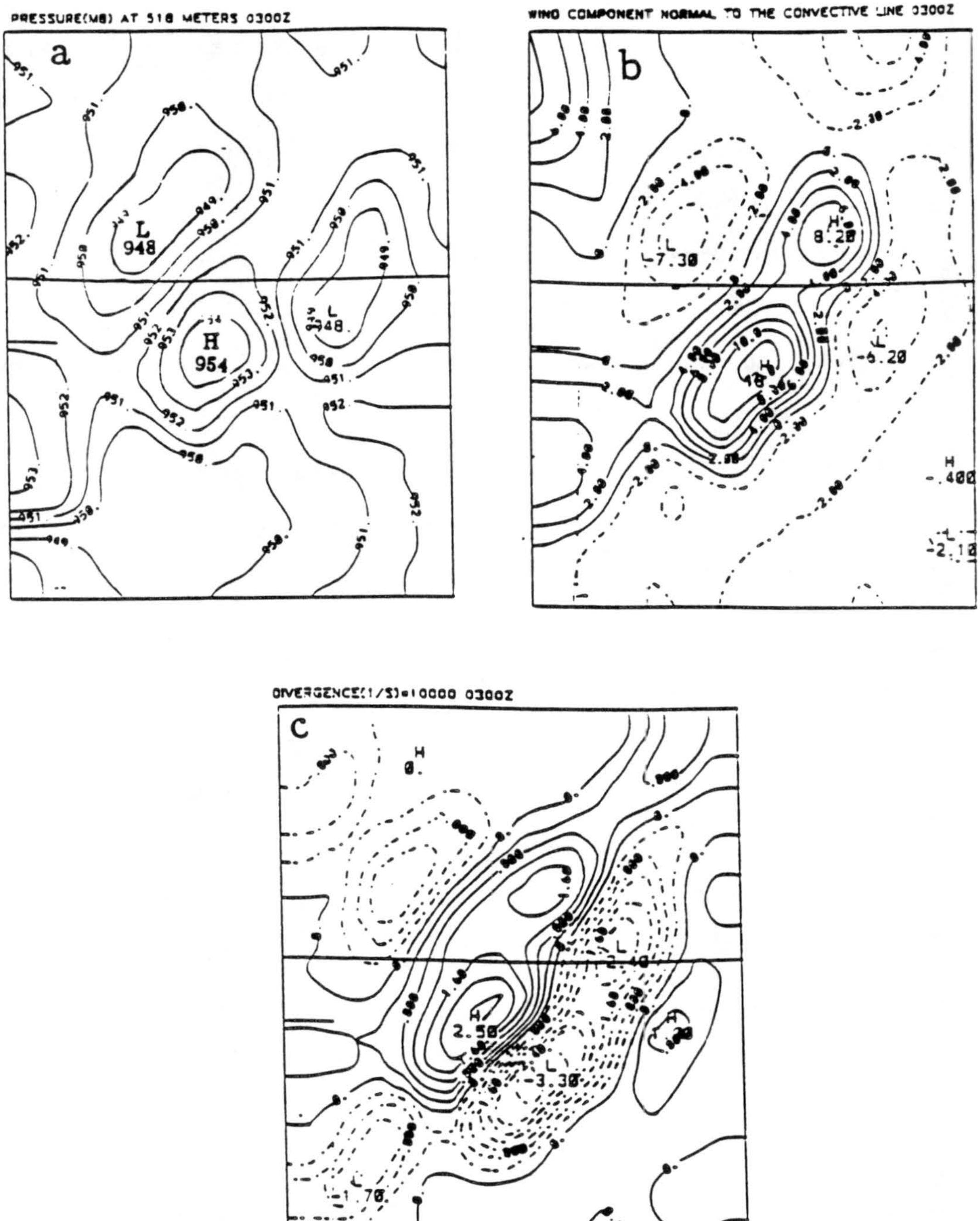

Figure 6.8: Same as Fig. 6.6, except for 0300 UTC.

slightly in magnitude by 0300. Although the convergence to the rear of the wake low increased in areal coverage by 0300, maximum convergence values essentially remained constant.

Finally, by 0400 (Fig. 6.9) , three distinct centers of maximum positive components were located just ahead of the mesohigh (which now had a central pressure of 955 mb) and the persistent pressure ridge extending northeast from the high center (denoted by the 952 mb contour). The maximum positive component had dropped to 10.6 m s^{-1}. The negative components, associated with the wake low, decreased in areal coverage and magnitude by 0400, as the wake low began to weaken. The pressure gradient between the mesohigh and wake low was weakening, as the separation between these two features increased. The divergence field displays several divergence maxima to the rear of the mesohigh and ridge axis, although maximum values had decreased since 0300. The strong convergence along the gust front at 0300 was still present at 0400, but was showing signs of weakening. The convergence to the rear of the wake low was still relatively strong, and now had a magnitude similar to that occurring along the gust front.

Table 6.1 summarizes the discussion of this section. The upper portion of the table lists the amplitude (refer to section 3.2.1 and fig. 3.1 to see how this value was determined), the maximum positive and negative wind components, the maximum divergence, and the maximum convergence associated with the pressure wave from 0100-0400 on the 11th. The amplitude of the pressure wave ranged from 2.5-3.5 mb, the maximum positive component from 8.1-13.4 m s^{-1}, the maximum negative component from 4.4-7.3 m s^{-1}, the maximum divergence 1.9-2.5 $\times 10^{-4}$ s^{-1}, and the maximum convergence from 2.3-3.3 $\times 10^{-4}$ s^{-1}. The maximum values of all of these parameters occurred at 0300 when the MCS was most intense.

The bottom portion of table 6.1 displays the separation or *phase shift* between the pressure and wind fields, as well as, the pressure and divergence fields for this particular mesoscale pressure wave. To determine the phase shift the following procedure was followed:

- A straight line oriented from 040° to 220° (which was the approximate orientation of the convective line) was drawn through the center of the pressure fields.

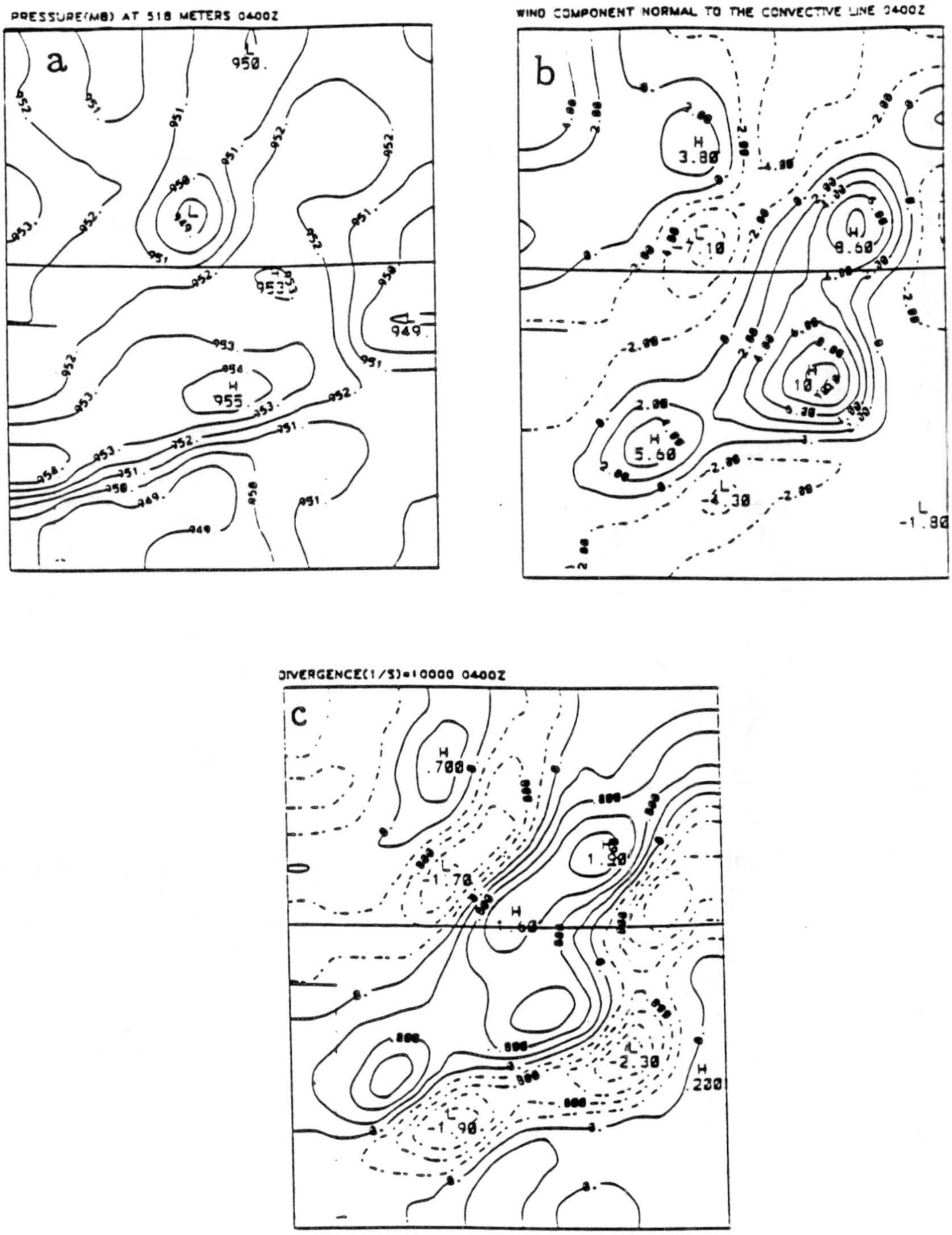

Figure 6.9: Same as Fig. 6.6, except for 0400 UTC.

Table 6.1: Observations of 11 June 1985.

TIME (UTC)	PRESSURE AMPLITUDE (mb)	MAX POSITIVE COMPONENT (m/s)	MAX NEGATIVE COMPONENT (m/s)	MAX DIVG. *10000 (1/s)	MAX CONV. *10000 (1/s)
0100	2.50	10.09	4.40	2.20	2.90
0200	2.50	8.10	5.50	1.90	2.50
0300	3.50	13.40	7.30	2.50	3.30
0400	3.00	10.60	7.10	1.90	2.30

SEPARATION(km) OF THE FOLLOWING:

TIME (UTC)	PRESSURE VS. DIV. MAX MAX	PRESSURE VS. CONV. MIN MAX	PRESS MAX VS. MAX POSITIVE COMP.	PRESS MAX VS. MIN NEGATIVE COMP.
0100	+34.90	—	-5.00	—
0200	+29.90	+45.00	0.00	-10.50
0300	+28.47	+28.50	-12.60	-9.80
0400	+31.90	+27.10	-25.90	-11.20
AVG.	+31.30	+33.50	-10.90	-10.50

- Next, the field of comparison (*i.e.* the wind and divergence fields) was placed over the pressure field.
- A perpendicular line was then drawn from the maximum in the field of comparison to the 040° to 220° line intersecting the pressure field.
- The horizontal distance represented by this line was found by breaking the line into its x and y components which correspond to a longitudinal (Δ_{lon}) and latitudinal (Δ_{lat}) distance in degrees, where a degree of latitude = 111.1 km, while a degree of longitude = 89 km (which is the longitudinal spacing at 36.75° N, the center latitude of the objective analysis grid).

The separation S was found by using the following equation:

$$S = ({\Delta_{lon}}^2 + {\Delta_{lat}}^2)^{\frac{1}{2}} . \tag{6.1}$$

Table 6.1 indicates that the maximum divergence was an average distance of 31.3 km to the rear of the mesohigh, the maximum convergence 33.5 km to the rear of the wake low, the maximum positive component 10.9 km ahead of the mesohigh, and the maximum negative component 10.5 km ahead of the wake low. The only phase relationship that exhibited great variability was the location of the maximum positive component relative to the mesohigh. Referring back to figs. 6.1-6.7, the pressure field, associated with the mesohigh, had a wide variety of shapes from nearly spherical at 0100 and 0300, to a high eccentricity ellipse at 0400. The rapidly changing pressure field may have prevented the development of a steady-state separation. These observed phase shifts will be compared to the model phase shifts in the next chapter.

6.3 Time series of pressure and wind direction at station PAM27

Another way to determine the characteristics of this mesoscale pressure wave is to construct a time series of pressure at a station that experienced the passage of both the mesohigh and wake low. For this case, one such station was PAM27 (labeled as P27 in fig. 5.2). Figure 6.10 displays a four hour time series of pressure and wind direction at P27.

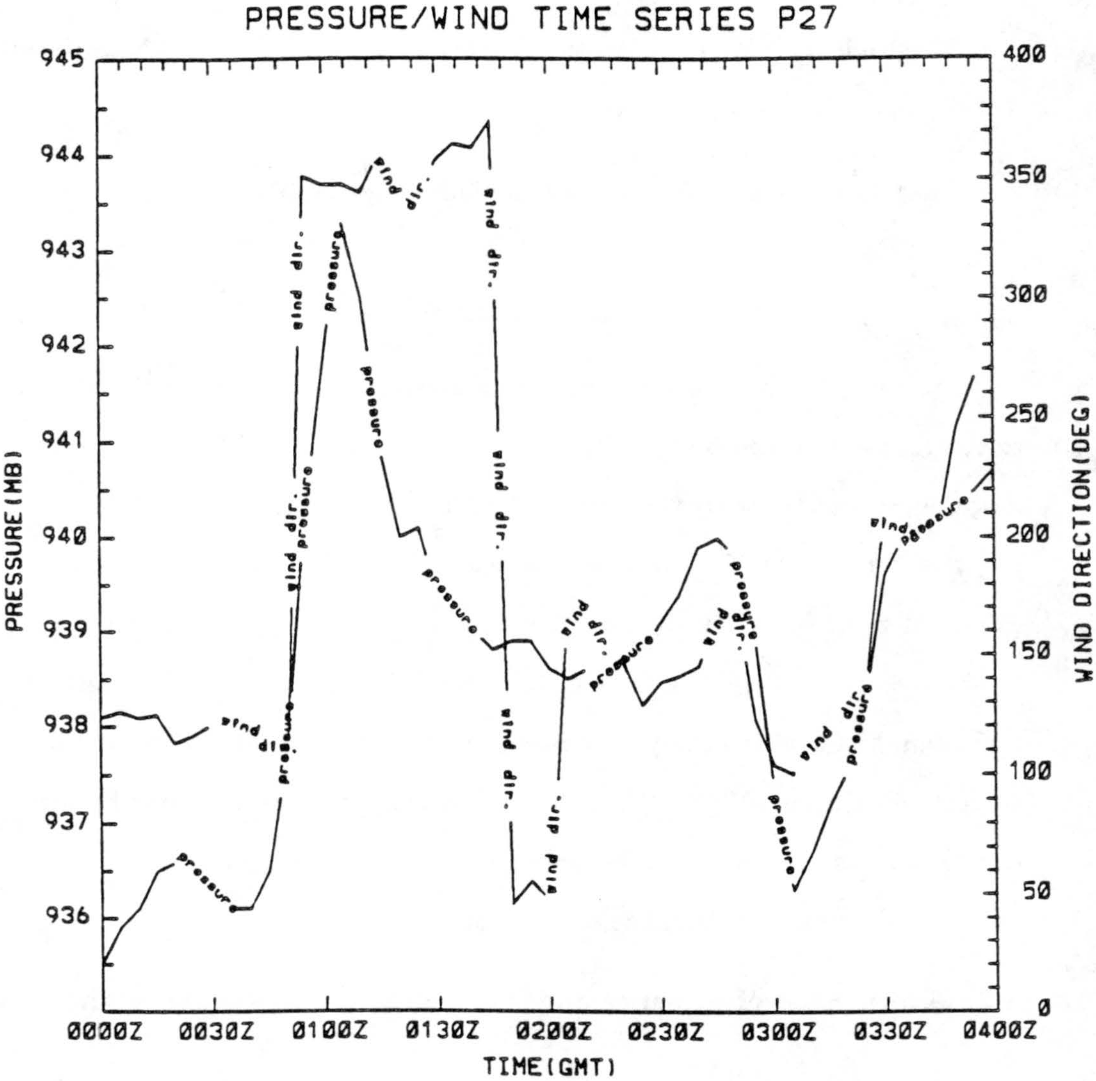

Figure 6.10: Time series of pressure (mb), and wind direction (degrees) for PAM27 (P27).

During this time, the station experienced the passage of the mesohigh and wake low. This figure was constructed using the 5 min averages of station pressure and wind direction recorded at P27.

At about 0040, the pressure at P27 began to rise very rapidly as the mesohigh began to surge through. During the next 25 min a pressure rise of 7 mb was reported. Moreover, a pressure rise of 2.5 mb in 5 min occurred between 0050 and 0055. This rapid pressure rise was referred to as a *pressure jump* by Tepper (1950) and *pressure surge* by Fujita (1955). After the mesohigh passage, the pressure dropped off rapidly to a level slightly above those recorded prior to its passage, until about 0230. After this time, the pressure began to rise just ahead of the wake low. Beginning at 0250, a sharp pressure drop occurred at the station as the wake low moved into the area. The pressure fell 3.5 mb between 0250 and 0305, and 1.5 mb in 5 min between 0255 and 0300. The wake low center passed the station at 0305, and was followed by a sharp pressure rise.

An examination of the wind's response to these MPF's shows that the flow was highly ageostrophic. For example, the wind direction at P27 veered from east- southeast to north-northwest as the mesohigh approached the station. This is to be expected since the wind normally veers as a high pressure builds into a region from the northwest. However, as the high moved to the southeast of P27, the wind did not back to the southwest. In fact, the wind continued to veer until 0200, which was 55 min *after* the center of the mesohigh passed this location. Between 0200 and 0205, the wind direction switched rapidly to south-southeast, where it generally remained until the wake low approached. Just prior to the wake low's passage, the wind shifted to the southeast. Once the low passed the station at 0305, the wind veered to southerly by 0330. Normally, when a surface low, that is in geostrophic balance, passes a particular location, the wind flow has a northerly component. This was not the case with this wake low, as the winds never veered to the north of west. In summary, the north winds to the rear of the mesohigh, and the south winds to the rear of the wake low indicate (as did the previous section) that air is flowing *through* these systems.

Chapter 7

A COMPARISON OF THE MODEL RESULTS WITH THE OBSERVATIONS

This chapter compares model results with the observations from the 10–11 June MCS. In this comparison, model results for the 2.5 mb wave are used, because the phase speed and amplitude of this wave are approximately equal to that observed with the MCS. Since the model did not use the actual surface data from this case, identical results are not expected. Although some quantitative comparisons are presented, most of the discussion is qualitative in nature. The model's ability to represent the general flow pattern associated with these MPF's is the most important consideration.

7.1 Comparison of wind and divergence fields

Table 7.1 displays the maxima in the model derived wind and divergence fields, as well as the fields observed with the MPF's associated with the 10–11 June MCS. The observations show that the maximum negative components, associated with the wake low, increased from 4.4 m s^{-1} at 0100 (when the wake low was just developing), to 7.3 m s^{-1} by 0300 (when the wake low was greatest in areal extent). The model results, for the wake low, show the same trend, but with a greater increase. Maximum easterlies (which are analogous to the maximum negative components) increase from 1.5 m s^{-1} at t= 30 min to 11.5 m s^{-1} at t =120 min. Since the station spacing in the PAM network is roughly 50 km, it is possible that wind speeds close to those predicted by the model may have occurred between reporting stations. The maximum convergence from the observations, during the time period of interest, was located ahead of the mesohigh along the gust front. Figures 6.6–6.9 indicate that the maximum convergence to the rear of the wake low was initially .8 $\times$ 10^{-4} s^{-1} at 0100. After this time, the maximum convergence remained

Table 7.1: Upper portion displays the maxima in the model derived wind and divergence fields for the 2.5 mb pressure wave at t = 30, 60, 90, and 20 min. The lower portion displays the maxima in the observed wind and divergence fields in one hour intervals from 0100–0400 UTC on the 11th.

TIME (MIN)	PRESSURE AMPLITUDE (mb)	MAX WESTERLY COMPONENT (m/s)	MAX EASTERLY COMPONENT (m/s)	MAX DIVG. *10000 (1/s)	MAX CONV. *10000 (1/s)
30	.62	1.3	1.5	.47	.73
60	1.25	4.4	5.2	1.52	1.91
90	1.87	7.2	8.9	2.47	4.76
120	2.50	10.9	11.5	3.18	5.76

TIME (UTC)	PRESSURE AMPLITUDE (mb)	MAX POSITIVE COMPONENT (m/s)	MAX NEGATIVE COMPONENT (m/s)	MAX DIVG. *10000 (1/s)	MAX CONV. *10000 (1/s)
0100	2.50	10.09	4.40	2.20	2.90
0200	2.50	8.10	5.50	1.90	2.50
0300	3.50	13.40	7.30	2.50	3.30
0400	3.00	10.60	7.10	1.90	2.30

between 1 and 2 $\times$ 10^{-4} s^{-1}. Convergence to the rear of the wake low, in the model, was initially .73 $\times$ 10^{-4} s^{-1} at t=30 min. By t = 60 min, the maximum convergence to the rear of the wake low was approximately equivalent to the maximum observed convergence. After t = 60 min, the maximum convergence in the model increased well beyond what was observed. By t = 120 min, the maximum convergence was 5.76 $\times$ 10^{-4} s^{-1}. Despite the large discrepancy in values of maximum convergence, the model results are still believable. In fact, one should expect the convergence to the rear of the wake low to increase as the low intensifies. The central pressure in the observed wake low remained nearly constant after 0130, indicating that this feature was not intensifying. This may explain why the convergence to the rear of this feature did not increase significantly with time.

Since the mesohigh was well developed by 0100, model results at t = 120 min were used to compare with observations since, at this time, the model pressure wave reached its maximum amplitude. Maximum observed positive components ranged from 8.1 m s^{-1} at 0200, to 13.4 m s^{-1} at 0300. These values agree quite well with the model's maximum westerly component (which is analogous to the maximum positive component) of 11.5 m s^{-1}. The maximum divergence to the rear of the mesohigh, was the same magnitude as the maximum observed divergence, but slightly larger. The maximum divergence in the model reached 3.18 $\times$ 10^{-4} s^{-1} at t = 120 min, while the maximum observed divergence was 2.5 $\times$ 10^{-4} s^{-1} at 0300. This difference is not significant, and the observed divergence may have been somewhat larger on a scale smaller than the horizontal resolution of 50 km.

7.2 A comparison of the phase shifts

Table 7.2 displays the phase shifts for the observations and the model. The best correlation between model results and observations occurs when comparing the average separation between the wake low and the convergence maximum to the rear. The model has an average separation of 30 km, while the observations show a 33.5 km average separation. As far as the remaining phase shifts are concerned, the differences are somewhat greater. However, the model accurately depicts the general flow pattern associated with the MPFs. Both the model and the observations show the following features:

Table 7.2: The upper portion displays the *phase shift*, or separation, of the maximum u-component (positive and negative), divergence, and convergence relative to the mesohigh and wake low axes in the 2.5 mb pressure wave. The lower portion displays the observed phase shifts associated with the mesoscale pressure fields on June 11th.

SEPARATION(KM) OF THE FOLLOWING:

TIME (MIN)	PRESSURE MAX VS. DIV. MAX	PRESSURE MIN VS. CONV. MAX	PRESSURE MAX VS. WESTERLY MAX	PRESSURE MIN VS. EASTERLY MAX
30	+10.0	+10.0	-27.5	-40.0
60	+17.5	+25.0	-17.5	-27.5
90	+25.0	+37.5	-17.5	-20.0
120	+22.5	+47.5	-17.5	-17.5
AVG.	+18.8	+30.0	-20.0	-26.3

TIME (UTC)	PRESSURE MAX VS. DIV. MAX	PRESSURE MIN VS. CONV. MAX	PRESS MAX VS. MAX POSITIVE COMP.	PRESS MIN VS. MAX NEGATIVE COMP.
0100	+34.90	—	-5.00	—
0200	+29.90	+45.00	0.00	-10.50
0300	+28.47	+28.50	-12.60	-9.80
0400	+31.90	+27.10	-25.90	-11.20
AVG.	+31.30	+33.50	-10.90	-10.50

- The maximum positive components are found ahead of the mesohigh.
- The maximum negative components are located ahead of the wake low.
- The maximum divergence occurs to the rear of the mesohigh
- The maximum convergence, associated with the wake low (*i.e.* excluding the convergence along the gust front), occurs to the rear of the low center.

In summary, agreement between model results and the observations for the 10–11 June squall line case is qualitatively, and in some instances even quantitatively, very good. Disagreements can probably be attributed to the model approximations and some observational limitations which are discussed in the next section.

7.3 Model approximations and observational limitations

In this section several model approximations and some observational limitations are discussed, which are the likely cause of some of the deviations between the model results and observations.

7.3.1 Model approximations

The major model approximations pertain to the treatment of the pressure field. These approximations are listed below:

1. The model pressure wave was only an approximation to the observed pressure field. The model pressure wave was sinusoidal, whereas the observed pressure wave (refer to Figs. 3.1–3.4) had much more structure than a simple sine wave.
2. Since the model pressure wave was sinusoidal, the strength, or amplitude, of the mesohigh and wake low were identical throughout the model run. This was not the case with the observations. The wake low developed well after the formation of the mesohigh.
3. In the model, the mesohigh and wake low moved at the same speed. The speed was determined by density current arguments which dictate the movement of the

mesohigh. In reality, the mesohigh moves as a density current, but the movement of the wake low is likely controlled by the interaction of the rear inflow jet with the stratiform rain area. This is shown in the observations. The mesohigh moved steadily southeast with the convective line, while the wake low moved more slowly to the east-southeast. The separation between these two features increased with time (refer to Fig. 6.5).

4. Finally, the model pressure wave amplified with every time step. The observations show no such trend. In fact, these features underwent periods of strengthening *and* weakening during the time period of interest.

Other approximations, not related to the pressure field, include:

1. The neglect of the Coriolis force. The timescale for this force ($\frac{1}{f}$) varies with latitude. At 30° the timescale is 3.8 hrs, and at 45° the timescale is 2.7 hrs. Since the model was run to only 2.5 hrs, only small errors, if any, may have occurred by neglecting this force.

2. The surface friction term included a drag coefficient that was approximated under statically neutral conditions. In reality, the atmosphere is statically stable near the surface over most of the squall line domain. Therefore, the drag coefficient used in the model may have been too large. However, it will be shown in the next chapter that the model is not highly sensitive to surface friction, therefore the choice of drag coefficient was not extremely critical.

7.3.2 Observational limitations

The observational limitations were less than the model limitations. Nonetheless, these limitations may have contributed to the deviations in the model derived wind field from the observed wind field. The following is a list of the observational limitations:

1. The spatial resolution of the observations was 50 km. This was sufficient to resolve the basic characteristics of the mesoscale pressure fields, and the wind flow associated with them. However, maximum (and minimum in the case of pressure) values of

pressure, wind speed, convergence, and divergence may have been located between stations. Therefore, errors in the position and magnitude of these features might have occurred.

2. Positional errors of these features would cause errors in the separation, or phase shift measurements discussed in section 6.2. With a 50 km spatial resolution, errors in separation might have been as large as 20 km.

To quickly summarize, the limitations of the model and the observations prevented a detailed quantitative comparison. However, since the model pressure wave was basically the same as that observed, model results were qualitatively quite similar to the observations.

Chapter 8

MODEL SENSITIVITY TO FRICTION

In this chapter the importance of surface friction will be examined through a scale analysis of the momentum equation. The model's sensitivity to the surface friction term will also be discussed. Finally, the role of momentum transport into the boundary layer from above is considered.

8.1 Scale analysis of the momentum equation with surface friction

To assess the relative importance of the surface friction term (hereafter referred to as friction term or friction), a scale analysis of the momentum equation is useful. Rewriting (2.3) with the friction term approximated by the first term on the RHS of (3.7), and $1/\rho = \alpha$ gives

$$\frac{\partial u}{\partial t} = -u\frac{\partial u}{\partial x} - \alpha\frac{\partial p}{\partial x} - C_D\frac{|u|\,u}{H} . \tag{8.1}$$

It is convenient to write (8.1) in terms of scaling variables where $u \sim U$, $x \sim L$, $p \sim \hat{p}$, $\alpha \sim \alpha_o$, and $t \sim \tau$. Equation (8.1) can now be written as:

$$\frac{U}{\tau} = -\frac{U^2}{L} - \alpha_o\frac{\hat{p}}{L} - C_D\frac{U^2}{H} . \tag{8.2}$$

Using the approximations that $\frac{C_D}{H} \sim 10^{-5}$, $\frac{1}{L} \sim 10^{-4}$, and $\alpha_o \sim 1$, (8.2) can be written:[8]

$$\frac{U}{\tau} = -10^{-4}U^2 - 10^{-4}\hat{p} - 10^{-5}U^2 . \tag{8.3}$$

---

[8]Since a centered in space finite difference is used $L = 2\Delta x = 10\,km$.

In the early stages of the model run $U \sim 1$ and $\hat{p} \sim 10$. This makes $\frac{1}{\rho}\frac{\partial p}{\partial x}$ one order of magnitude larger than $u\frac{\partial u}{\partial x}$ and two orders of magnitude larger than $C_D\frac{|u|u}{H}$. Thus the friction term is smaller than any other term on the RHS of (8.1). As $t \rightarrow 2\ hrs.$, $U \sim 10$, and $\hat{p} \sim 100$. $\frac{1}{\rho}\frac{\partial p}{\partial x}$ is now the same order of magnitude as $u\frac{\partial u}{\partial x}$ and both terms are one order of magnitude larger than $C_D\frac{|u|u}{H}$. In either case, the friction term, while small, is not negligible since it is only one order of magnitude smaller than the next smallest term in (8.1). It is also important to point out that the advection term ($u\frac{\partial u}{\partial x}$) is only one order of magnitude smaller than the pressure gradient term ($\frac{1}{\rho}\frac{\partial p}{\partial x}$) during the early stages of the model run. As time progresses, the magnitude of these terms become equal. Therefore, based on this analysis, the neglect of the advection term by Garratt and Physick (1983) is questionable.

8.2 Model results with various magnitudes of the surface friction term

In the previous section it was shown that the friction term is smaller than the other terms in the momentum equation, but still important. Therefore, the solution to (2.3) will be different for different values of C_D and H. Table 8.1 displays maximum positive and maximum negative u-components (MP and MN), as well as maximum divergence and maximum convergence (MD and MC) for a given C_D and H. These values are the maximum values in the grid at $t = 150\,min.$ (which is the offset time in the model) for a 200 km pressure wave with a maximum amplitude of 2.5 mb.

To begin with, when C_D is held constant at .005 and H is increased from 500 to 1000 m, MP increases 2–3 %, MN and MD 1–2 %, and MC 2–4 %, for every 100 m increase in H. When H is held constant at 500 m and C_d is decreased from .005–.001, MP increases 4–6 %, MN and MD 2- -3 %, and MC 5–27 %, for every .001 decrease in C_D.

It appears that convergence is most sensitive to changes in the magnitude of the friction term[9]. In fact, when friction is eliminated MC is 101 % larger than MC when C_D = .005 and H = 500 m, whereas MD is only 38 % larger, MP 30 %, and MN 13 %. The

[9]The location of maximum convergence may be located along the simulated gust front ahead of the mesohigh, rather than to the rear of the wake low, especially towards model offset time.

Table 8.1: Comparison of the maxima in the wind and divergence fields for various magnitudes of the friction term. C_d = the surface drag coefficient, and H = the boundary layer depth in meters. Values listed are valid at t = 150 min for a 2.5 mb amplitude pressure wave with a phase speed = 16.3 m s^{-1}.

FRICTION	MAX POSITIVE COMPONENT (m/s)	MAX NEGATIVE COMPONENT (m/s)	MAX DIVERGENCE *10000(1/s)	MAX CONVERGENCE *10000(1/s)
Cd = .005 H = 500 m	14.6	-12.6	3.53	5.97
Cd = .005 H = 600 m	15.1	-12.8	3.59	6.20
Cd = .005 H = 700 m	15.5	-13.0	3.65	6.37
Cd = .005 H = 800m	15.8	-13.2	3.69	6.50
Cd = .005 H = 900 m	16.1	-13.3	3.73	6.61
Cd = .005 H = 1000 m	16.4	-13.4	3.76	6.75
Cd = .004 H = 500 m	15.2	-12.9	3.61	6.24
Cd = .003 H = 500 m	15.9	-13.2	3.70	6.54
Cd = .002 H = 500 m	16.8	-13.5	3.81	7.68
Cd = .001 H = 500 m	17.8	-13.9	3.94	9.78
No Friction	19.0	-14.3	4.68	12.01

very large increase in MC is due to an increasing gradient of u along the gust front as friction is reduced. The wind speed just ahead of the gust front is allowed to increase, but several km ahead of the gust front, where the pressure gradient is flat, the wind remains calm.

8.3 The importance of momentum transport

The second term on the RHS of eq. (3.7) refers to the momentum flux, $(\overline{u'w'})$, at the top of the model layer. A first attempt was made to parameterize this term as a function of the vertical wind shear. Therefore, $(\overline{u'w'}) = -K_m \frac{\partial a}{\partial z}$, where K_m = exchange coefficient for momentum. Pielke (1984) developed an expression to determine K_m:

$$K_m = 1.1(Ri_c - Ri)l^2 \frac{\left|\frac{\partial a}{\partial z}\right|}{Ri_c}; \quad Ri \leq Ri_c \ , \tag{8.4}$$

where Ri = gradient Richardson number, Ri_c = critical Richardson number = 0.25, and l = mixing length. In (8.4), $l = 70\ m$ if z (or H in this case)$\geq 200\,m$. If $Ri \geq Ri_c$, $K_m = 0$ and there is no momentum transport.

The gradient Richardson number is essentially buoyant production of turbulent kinetic energy (TKE) divided by shear production of TKE and can be written as follows:

$$Ri = \frac{g}{\theta_{v_o}} \frac{\frac{\partial \theta_v}{\partial z}}{(\frac{\partial a}{\partial z})^2} \ , \tag{8.5}$$

where θ_v = virtual potential temperature, and θ_{v_o} = surface virtual potential temperature. If one assumes that $\frac{\partial q}{\partial z} \sim 0$ (which is a good assumption in a well mixed boundary layer), $\frac{\partial \theta_v}{\partial z} \sim \frac{\partial \theta}{\partial z}$ and (8.5) can be written

$$Ri = \frac{g}{\theta_{v_o}} \frac{\frac{\partial \theta}{\partial z}}{(\frac{\partial a}{\partial z})^2} \ . \tag{8.6}$$

Dodge City Kansas (DDC) rawindsonde data at 0238Z on the 11th were used to calculate Ri (See Fig. 8.1 for a sounding plot). The convective line had just passed DDC. The surface temperature $(T_o) = 290.35K$, and the surface virtual temperature $(T_{v_o}) = 292.4K$. With this information θ_o and θ_{v_o} can be found using Poisson's equation. Since

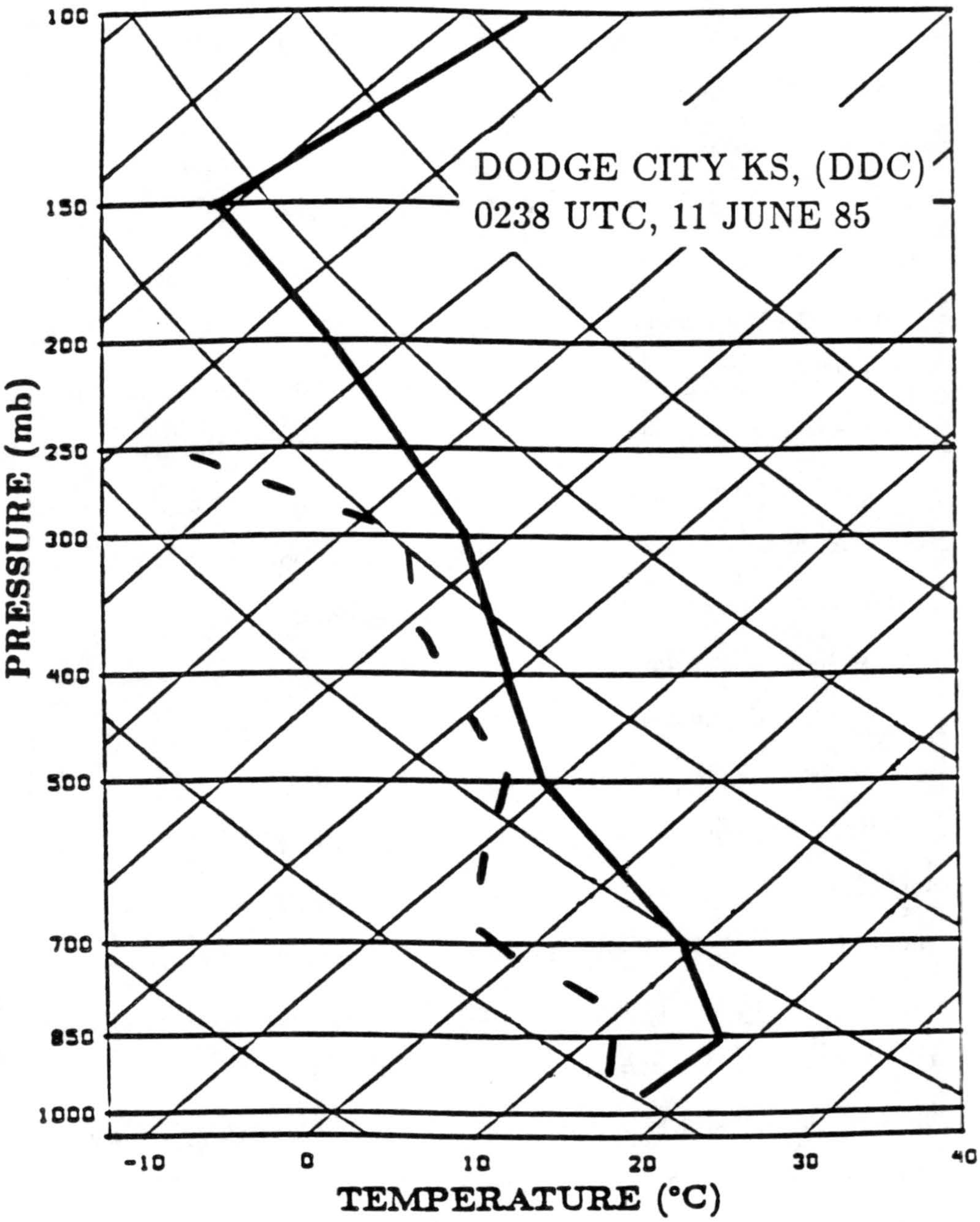

Figure 8.1: A temperature (solid curve) and dewpoint (dashed curve) ($°C$) sounding for Dodge City Kansas (DDC) at 0238Z on the 11th.

the model used an H of 500 m when comparing model results with observations, the potential temperature at 500 m at DDC was used to get a value of $\frac{\partial\theta}{\partial z}$. A value of $\frac{\partial u}{\partial z}$ within the first 500 m of the surface $= .004\,s^{-1}$ was taken from Fig. 4.2 of Gallus (1989). Using these values for the variables in (7.6), $Ri = 28.67$. Therefore, the use of (8.4) with observed mean shears leads to the conclusion that $K_m = 0$, which means that there is no momentum transport.

The above analysis, however, is probably not appropriate in the region of the convective line where convective scale updrafts/downdrafts are occurring. For this reason, the momentum transport term, $\overline{u'w'}$, was applied to the first $\frac{1}{4}\lambda$ of the pressure wave (which is analogous to the region of the convective line). The value for $\overline{u'w'}$ was taken from LeMone *et al.* (1984). They used a $\overline{u'w'} = -.768$ m^2 s^{-2} for MCSs moving at 11–14 m s^{-1}, which is close to the speed of the MCS being studied here. In the model, $\overline{u'w'}$ was set to 0 at $t = 0$, and increased linearly to LeMone *et al.'s* value of momentum transport at $t = 2$ hrs.

Figure 8.2a displays model pressure and u-component, while fig. 8.2b is a plot of model pressure and divergence for the case where momentum transport is included. Both are at $t = 120$ min for a model run with a pressure wave whose maximum amplitude is 2.5 mb and phase speed = 16.3 m s^{-1}. These conditions are identical to a model run discussed in chapter 4. (see fig. 4.4 for results of this run at $t = 120$ min without momentum transport), except that momentum transport, at the model layer top, was included in the momentum equation in the manner described above. The addition of momentum transport produced changes in the wind field near the mesohigh. Since $\overline{u'w'}$ is negative, momentum transport caused an increase in westerly winds at the surface. This is reflected by a maximum u-component = 14.9 m s^{-1}, when momentum transport was included, as opposed to a maximum u-component = 10.9 m s^{-1} when it was not. As a result, convergence ahead of the mesohigh increased from 4.33 to 6.30×10^{-4} s^{-1}. Also, divergence to the rear of the mesohigh increased from 3.18 to 3.92×10^{-4} s^{-1} since air ahead of the mesohigh axis is accelerated, while air to the rear is not.

As far as phase relationships are concerned, when momentum transport was included, the maximum u-component was located 5 km ahead (i.e. in the positive x-direction) of

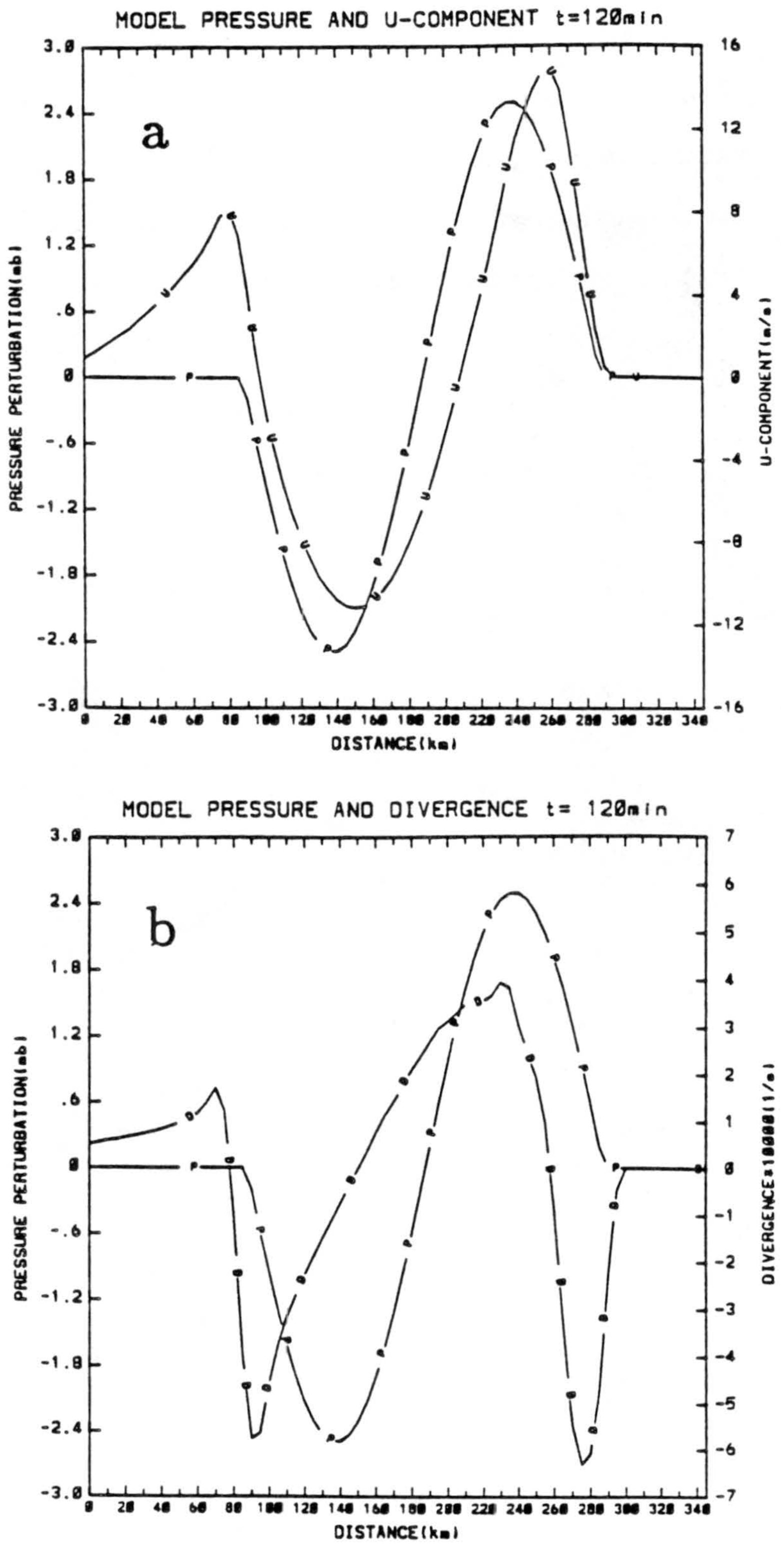

Figure 8.2: Same as Fig. 4.4, except that convective transport is included.

where it was found when momentum transport was not considered. This caused the location of maximum convergence to shift 5 km ahead as well. The maximum divergence was shifted 15 km ahead and was within 7.5 km the mesohigh axis.

In summary. momentum transport by convective scale updrafts and downdrafts may serve to enhance the westerly flow and convergence along the gust front. However, behind the convective line this effect is minimized due to the high stability of the rain-cooled air.

Chapter 9

SUMMARY

This study used a simple one-dimensional slab model to simulate the wind's response to transient mesoscale pressure fields that often accompany midlatitude squall lines. The model solves the finite difference approximation to a form of the momentum equation which includes the pressure gradient force, advection and the frictional force. A coordinate system was adopted such that u was the line-normal component relative to the pressure fields. The line-parallel component was considered small in comparison, and was therefore neglected. This modeling approach was similar to that applied by Garratt and Physick (1983). The pressure field in the model was comprised of a sinusoidal pressure wave propagating at a constant phase speed through a flat environmental pressure gradient. The phase speed of the wave was determined under the assumption that it moved as a density current. Thus, the phase speed of the wave was proportional to the square root of its amplitude (Seitter, 1986). This pressure wave is analogous to a mesohigh and a wake low that have the same amplitude and phase speed. The amplitude of the pressure wave was initially zero, but then increased linearly with every timestep until the wave's maximum amplitude was reached at t = 120 min. The gradual build up of the pressure amplitude prevented the occurrence of instabalities in the wind field.

Model results agree quite well with the schematic displayed in Fig. 1.3 (Johnson and Hamilton, 1988). In the simulated wind field, the instantaneous airflow was directed forward through the mesohigh and rearward through the wake low. An axis of divergence was located to the rear of the mesohigh, with convergence occurring ahead of the mesohigh along the gust front, and at the back edge of the wake low. The model was run using pressure waves with various maximum amplitudes (hence various phase speeds). Regardless of the wave's maximum amplitude, the wind field was similar to that depicted in Fig. 1.3. However, as the maximum amplitude (and phase speed) of the pressure wave increased several trends in the wind field were discovered.

First, as the maximum amplitude of the pressure wave increased, the maximum u-components (both positive and negative) increased. This makes physical sense since stronger pressure gradients accompany the higher amplitude wave. Wind speeds were not as high as expected because the higher amplitude pressure wave moved more quickly than its slower counterparts. Therefore, air parcels spent less time in a pressure gradient favorable for continued acceleration. It was shown that the stronger wind speeds, that occur with a higher amplitude wave, produce locally stronger wind speed gradients than those occurring with lower amplitude waves. The stronger wind speed gradients produced higher values of convergence and divergence. The only exception to this trend occurred at the rear of a 1.5 mb amplitude wake low. The convergence at the back edge of this low was stronger than that occurring with a 2.5 or 3.5 mb wake low. This is an important finding since the magnitude of convergence, to the rear of the wake low, may not be proportional to the low's strength. Air parcels had a higher residence time at the back edge of this low, than in the other two waves. Thus, wind speeds at the back edge of the low eventually exceeded those located at the back edge of the other wake lows, despite the weaker pressure gradient. The stronger wind speeds caused stronger convergence to the rear of this lower amplitude wake low.

Model results also indicate that the strongest positive and negative u- components (west and east winds) occur several km ahead of the mesohigh and wake low respectively, rather than right near the center of these features. This too was explained by air parcel trajectories. Individual air parcels reached their maximum speed within 1-3 km of the pressure centers. However, a second parcel, that entered the wave at a later time, experienced a stronger pressure gradient since the model pressure wave amplified with time. Therefore, as the first parcel reached its maximum speed just ahead of the pressure center, the second parcel had already attained a higher speed than the first, despite being a considerable distance from the center of either the wake low or mesohigh.

Finally, model results indicated that as the phase speed of the wave increased, the maximum convergence and divergence occurred farther to the rear of the wake low and mesohigh centers respectively. Air parcel trajectories indicated that positive u-components extended farther to the rear of the mesohigh, while negative u-components extended farther to the rear of the wake low, as the phase speed of the pressure wave increased. This shifted the convergence and divergence centers further behind the wake low and mesohigh respectively.

The model derived wind field was compared in a qualitative manner to observations of the wind field near the mesohigh and wake low associated with an intense squall line that moved through Kansas and Oklahoma on 10-11 June 1985. Model results compare well with the observations considering the the model approximations and observational limitations discussed in Section 7.3. Both the model and the observations showed that the maximum positive components occurred ahead of the mesohigh, maximum negative components were found ahead of the wake low, maximum divergence occurred to the rear of the mesohigh, and maximum convergence was located to the rear of the wake low.

A scale analysis of the momentum equation, as well as a sensitivity test, were conducted to assess the relative importance of the surface friction term. The scale analysis showed that the friction term was not small enough, relative ot the other terms in the momentum equation, to be neglected. The sensitivity test indicated that slightly different solutions occurred as the magnitude of the friction term was varied. The relative importance of momentum transport, from above the model layer, was also discussed. It appears that such transport is only important near the convective line, where thunderstorm updrafts and downdrafts are occurring. Behind the convective line, the air is much too stable, and the penetrative drafts too weak to promote significant transport.

This study was one of the few that have investigated the surface airflow in in the vicinity of these surface pressure features. Future work may include the addition of the Coriolis force. This would allow for longer time integrations. Adding the y-dimension to the model would be useful in capturing the two-dimensional properties of these pressure fields. The development of a model that has vertical resolution could be used to determine if significant vertical wind shear is to be expected with these pressure features. Finally, a model with vertical resolution *and* precipitation physics could be used to simulate the airflow at mid-levels in the stratiform region. It could then be determined if a mesolow develops and initiates a rear-inflow jet in this area.

REFERENCES

Asselin, R., 1972: Frequency filter for time integrations. *Mon. Wea. Rev.*, **100**, 487–490.

Barnes, S. L., 1964: A technique for maximizing details in numerical weather map analysis. *J. Appl. Meteor.*, **3**, 396–409.

Brown, J. M., 1979: Mesoscale unsaturated downdrafts driven by rainfall evaporation: A numerical study. *J. Atmos. Sci.*, **36**, 313–338.

Byers, H. R., and R. R. Braham, 1949: The thunderstorm. U. S. Weather Bureau, Washington, D. C., 287 pp.

Brunk, I. W., 1953: Squall lines. *Bull. Amer. Meteor. Soc.*, **34**, 1–9.

Charba, J., 1974: Application of the gravity current model to analysis of squall-line gust fronts. *Mon. Wea. Rev.*, **102**, 140–156.

Courant, R., K. O. Friedrichs and H. Lewy, 1928: Uber die partiellen differenzengleichungen der mathematischen physik. *Math Annalen,* **100**, 32–74.

Cunning, J. B., 1986: The Oklahoma-Kansas Preliminary Regional Experiment for STORM–Central. *Bull. Amer. Meteor. Soc.*, **67**, 1478–1486.

Ellsaesser, H. W., 1966: Evaluation of spectral versus grid methods of hemispheric numerical weather prediction. *J. Appl. Meteor.*, **5**, 246–262.

Fritsch, J. M., and C. G. Chappell, 1980: Numerical prediction of convectively driven mesoscale pressure systems. Part II: Mesoscale model. *J. Atmos. Sci.*, **37**, 1734–1762.

Fujita, T. T., 1955: Results of detailed synoptic studies of squall lines. *Tellus,* **7**, 405–436.

Fujita, T. T., 1959: Precipitation and cold air production in mesoscale thunderstorm systems. *J. Meteor.,* **16**, 454–466.

Gallus, W. A., 1989: The heat, moisture, and momentum budgets of a midlatitude squall line with a trailing stratiform region. M.S. Thesis, Colorado State University Dept. of Atmos. Sci., 126 pp.

Garratt, J. R., and W. L. Physick, 1983: Low-level wind response to mesoscale pressure systems. *Bound.-Layer Meteor.*, **27**, 69–87.

Haltiner, G. J., and Williams, R. T., 1980: "Numerical Prediction and Dynamic Meteorology," 2nd edition. Wiley, New York.

Johnson, R. H., and P. J. Hamilton, 1988: The relationship of surface pressure features to the precipitation and air flow structure of an intense midlatitude squall line. *Mon. Wea. Rev.*, **116**, 1444–1472.

Koch, S. E., and J. McCarthy, 1982: The evolution of an Oklahoma dryline. Part II: Boundary-layer forcing of mesoconvective systems. *J. Atmos. Sci.*, **39**, 237–257.

Kubota, S., 1959: Surface spherical harmonic representations of the system of equations for analysis. *Papers Meteor. Geophys.* (Tokyo), **10**, 145–166.

Lavoie, R. L., 1972: A mesoscale numerical model of lake-effect storms. *J. Atmos. Sci.*, **29**, 1025–1040.

LeMone, M. A., G. A. Barnes and E.J. Zipser, 1984: Momentum flux by lines of cumulonimbus over the tropical oceans. *J. Atmos. Sci.*, **41**, 1914–1932.

Mahrt, L. J., 1974: Time-dependent, integrated planetary boundary layer flow. *J. Atmos. Sci.*, **31**, 457–464.

Newton, C. W., 1950: Structure and mechanisms of the pre-frontal squall line. *J. Meteor.*, **10**, 210–222.

Panofsky, H. A., and J. A. Dutton, 1984: "Atmospheric Turbulence." John Wiley & Sons, New York.

Pielke, R. A., 1984: "Mesoscale Meteorological Modeling." Academic Press, Orlando.

Pedgley, D. E., 1962: A meso-synoptic analysis of the thunderstorms on 28 August 1958. Brit. Meteor. Off., Geophys. Mem., No. 106, 74 pp.

Rutledge, S. A., R. A. Houze, Jr., M. I. Biggerstaff and T. Matejka, 1988: The Oklahoma-Kansas mesoscale convective system of 10–11 June 1985: Precipitation structure and single–Doppler radar analysis. *Mon. Wea. Rev.*, **116**, 1409–1430.

Sawyer, J. S., 1946: Cooling by rain as a cause of the pressure rise in convective squalls. *Quart. J. Roy. Meteor. Soc.*, **72**, 168.

Schaffer, W., 1947: The thunderstorm high. *Bull. Amer. Meteor. Soc.*, **28**, 351–355.

Seitter, K . L., 1986: A numerical study of atmospheric density current motion including the effects of condensation. *J. Atmos. Sci.*, **43**, 3068–3076.

Silberman, I., 1954: Planetary waves in the atmosphere. *J. Meteor.*, **11**, 27–34.

Simpson, J. E. 1969: A comparison between laboratory and atmospheric density currents. *Quart. J. Roy. Meteor. Soc.*, **95**, 758–765.

Simpson, J. E., D. A. Mansfield, and J. R. Milford, 1977: Inland penetration of sea breeze fronts. *Quart. J. Roy. Meteor. Soc.*, **103**, 47–76.

Smull, B. F., and R. A. Houze, Jr., 1987: Rear inflow in squall lines with trailing stratiform precipitation. *Mon. Wea. Rev.*, **115**, 2869–2889.

Stull, R. B., 1988: "An Introduction to Boundary Layer Meteorology." Kluwer, Norwell.

Stumpf, G. J., 1988: Surface pressure features associated with a mesoscale convective system in O. K. PRE-STORM. M.S. Thesis, Colorado State University Dept. of Atmos. Sci., 148 pp.

Tepper, M. 1950: A proposed mechanism of squall lines: The pressure jump line. *J. Meteor.*, **7**, 21–29.

Thompson, P. D., 1961: "Numerical Weather Analysis and Prediction." Macmillan, New York.

Wakimoto, R. M., 1982: The life cycle of thunderstorm gust fronts as viewed with Doppler radar and rawinsonde data. *Mon. Wea. Rev.*, **110**,, 1060–1082. Dept. of Atmos. Sci., 148 pp.

Williams, D. T., 1948: A surface micro-study of squall-line thunderstorms. *Mon. Wea. Rev.*, **76**, 239–246.

Williams, D. T., 1953: Pressure wave observations in the central Midwest, 1952. *Mon. Wea. Rev.*, **81**, 278–298.

Williams, D. T., 1954: A surface study of a depression-type pressure wave. *Mon. Wea. Rev.*, **82**, 289–295.

Williams, D. T., 1963: The thunderstorm wake of May 4, 1961. Nat. Severe Storms Project Rep. No. 18, U. S. Dept. of Commerce, Washington D. C., 23 pp. [NTIS PB 168223].

Zhang, D. L., K. Gao and D. B. Parsons, 1989: Numerical simulation of an intense squall line during 10–11 June 1985 PRE-STORM. Part I: Model verification. *Mon. Wea. Rev.*, **117**, 960–994.

Zipser, E. J., 1977: Mesoscale and convective-scale downdrafts as distinct components of squall line structure. *Mon. Wea. Rev.*, **105**, 1568–1589.